JOURNAL OF GEOPHYSICAL RESEARCH, VOL. 111, A10S12, doi:10.1029/2005JA011510, 2006

Influence of solar variability on gravity wave structure and dissipation in the thermosphere from tropospheric convection

Sharon L. Vadas[1] and David C. Fritts[1]

Received 1 November 2005; revised 22 March 2006; accepted 22 May 2006; published 22 September 2006.

[1] We investigate the role convection plays in the thermosphere using deep convection and ray trace models with a general dissipative anelastic GW dispersion relation. In the absence of dissipation, a GW's vertical wavelength λ_z increases by $\sqrt{\overline{T}/\overline{T}_0}$, or greater if its intrinsic frequency ω_{Ir} is close to the smaller thermospheric buoyancy frequency $N = \sqrt{\overline{T}_0/\overline{T}}\, N_0$. Here, $\overline{T}$ and $\overline{T}_0$ are the asymptotic temperatures in the thermosphere and lower atmosphere, respectively, and N_0 is the buoyancy frequency in the lower atmosphere. In the presence of dissipation, λ_z also increases in the thermosphere by a factor of $\sim$2–3 when $\omega_{Ir} > 0.2N_0$ and $\lambda_z > 25$ km during active solar conditions. GW dissipation altitudes and maximum vertical wavelengths, which increase as $\overline{T}$ increases, are displayed for small-scale and midscale GWs. GWs excited from deep convection encounter horizontal shears, which impose anisotropy on the spectrum. Along with dissipative filtering, momentum flux divergence and body forces result. The thermospheric body forces resulting from our convection model achieve maximum accelerations at $z \simeq 180$–200 km, extend down to $z \simeq 130$ km, last for the duration of deep convection, are $\sim$600 km $\times$ 600 km $\times$ 40–80 km in the x, y, and z directions, and are very strong with accelerations $\simeq$0.5–0.75 m s^{-2} and $\simeq$0.25–0.4 m s^{-2} during extreme solar minimum ($\overline{T}$ = 600 K) and active solar conditions ($\overline{T}$ = 2000 K), respectively. During extreme solar minimum, there is negligible forcing above $z \simeq 230$ km, whereas the forcing extends up to $z \simeq 360$ km during active solar conditions. These horizontal, thermospheric body forces may be a new source of large-scale, long-period secondary GWs and induced TIDs (traveling ionospheric disturbances) at high altitudes in the thermposphere.

Citation: Vadas, S. L., and D. C. Fritts (2006), Influence of solar variability on gravity wave structure and dissipation in the thermosphere from tropospheric convection, *J. Geophys. Res.*, *111*, A10S12, doi:10.1029/2005JA011510.

1. Introduction

[2] Over the past 4 decades, internal gravity waves (GWs) have been recognized to play major roles in atmospheric dynamics extending from Earth's surface into the mesosphere and lower thermosphere (MLT). Excited primarily by topography, convection, and wind shear, they span a wide range of frequencies and spatial scales, increase significantly in amplitude due to decreasing density with altitude, and exhibit a wide range of interactions and instabilities as a result of their amplitude increases with altitude. Their principal effects, however, derive from their significant and efficient transport of momentum and energy from source regions to regions where dissipation occurs. Interactions with the mean flow and low-frequency wave motions result (1) in closure of the mesospheric jets, (2) a GW-driven residual circulation from the summer to the winter hemisphere near the mesopause with rising motions and cooling in the summer mesosphere and subsidence and warming in the winter mesosphere, (3) modulations of tidal and planetary wave amplitudes in the MLT, and (4) mapping of these larger-scale motions to higher altitudes. Additionally, GW instability dynamics lead to significant turbulence, strong GW dissipation, and local body forcing that may exceed mean values by 1 or 2 decades in magnitude. These GW effects were reviewed in detail by *Fritts and Alexander* [2003].

[3] Most recent efforts to understand influences from lower atmospheric GWs have focused on the MLT and below. For example, GWs from severe storms have been observed not only in the stratosphere but also in airglow layers near the mesopause [*Taylor and Hapgood*, 1988; *Dewan et al.*, 1998; *Sentman et al.*, 2003]. Atmospheric GWs have been observed in the thermosphere and ionosphere for decades [e.g., *Hocke and Schlegel*, 1996; *Oliver et al.*, 1997; *Djuth et al.*, 1997, 2004]. Most of this research focused on observing and modeling excitation and propagation of large-scale GWs from auroral sources in the lower thermosphere at high latitudes [*Hocke and Schlegel*, 1996; *Hocke et al.*, 1996; *Richmond*, 1978; *Hickey and Cole*, 1988]. However, medium-scale GWs from lower atmospheric sources are also very frequently observed at midlatitudes in the thermosphere with periods less than an hour and phase speeds less than 250 m s^{-1} [*Waldock and Jones*,

[1]Colorado Research Associates, NorthWest Research Associates, Boulder, Colorado, USA.

0148-0227/06/2005JA011510$09.00

1986; *Crowley et al.*, 1987; *Ogawa et al.*, 1987; *Hocke and Schlegel*, 1996].

[4] Early theoretical work estimated the effect individual GWs would have on the thermosphere [*Hines*, 1960, 1967; *Pitteway and Hines*, 1963; *Francis*, 1973; *Yeh et al.*, 1975; *Richmond*, 1978; *Hickey and Cole*, 1987]. The influence of GWs from lower atmospheric sources such as convection, hurricanes, tornados, jet streams, and secondary waves from wave breaking near the mesopause are recognized to have potentially significant effects at these higher altitudes [*Bauer*, 1958; *Röttger*, 1977; *Hung et al.*, 1978; *Hung and Kuo*, 1978; *Hung and Smith*, 1978; *Waldock and Jones*, 1987; *Hocke and Tsuda*, 2001; *Vadas and Fritts*, 2002; *Fritts et al.*, 2002; *Vadas et al.*, 2003; R. Bishop et al., Arecibo observations of ionospheric perturbations associated with the passage of tropical storm Odette, submitted to *Journal of Geophysical Research*, 2006], and this influence is expected to vary seasonally due to the seasonal variation of the mesospheric winds and the tidal component in the lower thermosphere winds [*Hines and Reddy*, 1967; *Larsen*, 2002; *Larsen et al.*, 2003]. Even so, theoretical research in this area has been lacking. This is in part because there is a lack of observations tracking GW excitation and propagation from convection into the thermosphere. It is also in part due to the lack of theoretical modeling of GW excitation from lower atmospheric sources, propagation of these GWs into the thermosphere, and an accurate description of their dissipation within the thermosphere in a time- and space-dependent manner so as to capture the transient and localized thermospheric effects that these intermittent, spatially localized, and complicated GW sources have on the thermosphere.

[5] This paper focuses specifically on the influence of GWs from convection on the thermosphere. Key components of such theoretical modeling involve (1) a realistic, localized convection model which calculates the velocity and temperature amplitudes for short and long vertical wavelength GWs, and (2) a fast ray trace model which propagates these GWs from a small region of convection in the troposphere into a much larger volume in the thermosphere, where they dissipate in a spatially localized and intermittent manner. As to the first key component, many three-dimensional (3-D) numerical, nonlinear models of convection have been developed [*Lane et al.*, 2001; *Piani et al.*, 2000; *Horinouchi et al.*, 2002]. Although these models can calculate amplitudes and scales of GWs with small vertical wavelengths, they cannot accurately calculate amplitudes of GWs with very large vertical wavelengths due to upper boundary model limitations and the much smaller wave amplitudes involved. Those GWs with small vertical wavelengths will likely break near the mesopause, leading to momentum flux divergence, horizontal body forcing, and the reversal of the jets in the summer and winter mesosphere (see the review by *Fritts and Alexander* [2003]). Those GWs with large vertical scales and small amplitudes from the same convective sources, however, will propagate through the mesopause and into the thermosphere. Because it is the large-scale GWs which will most likely influence the dynamics of the thermosphere and ionosphere, an analytic model of convection was developed which reproduces the salient features of small-scale GW amplitudes and interference patterns near the mesopause, but also calculates the GW amplitudes for a wide range of scales which includes very large vertical wavelengths [*Vadas and Fritts*, 2004, hereinafter referred to as VF2004].

[6] As to the second key component of theoretical modeling, ray tracing these GWs into the thermosphere is needed in order to capture the intermittent and spatially complicated nature of convection and its effect on the thermosphere. In order to accurately ray trace GWs in the thermosphere, it is necessary to utilize a dispersion relation which includes realistic sources of thermospheric dissipation. Until recently, GW propagation in the thermosphere with dissipation was mainly accomplished with multilayer techniques [*Midgley and Liemohn*, 1966; *Volland*, 1969b; *Klostermeyer*, 1972; *Hickey and Cole*, 1988], numerical simulations [*Richmond*, 1978; *Francis*, 1973; *Zhang and Yi*, 2002], and approximate or numerical solutions to complex dispersion relations [*Pitteway and Hines*, 1963; *Yeh et al.*, 1975; *Hickey and Cole*, 1987]. Recently, an analytic, anelastic, GW dispersion relation which includes molecular viscosity and thermal conductivity more accurately was derived [*Vadas and Fritts*, 2005, hereinafter referred to as VF2005]. This dispersion relation is real and was derived from the more general complex dispersion relation by assuming a complex intrinsic frequency and real vertical wave number. This dispersion relation allows for the accurate ray tracing of GWs from the lower atmosphere into the thermosphere and ionosphere when ion drag and wave-induced diffusion can be neglected. Recently, this dispersion relation with molecular viscosity only, coupled with the previously mentioned analytic convection model, was used to explore the effects of mesoscale convective complexes (MCCs) on the thermosphere (VF2004). Although this study utilized an unrealistic isothermal background temperature in the thermosphere and underrepresented the effects of dissipation, these authors extrapolated their results to more realistic conditions and were able to anticipate potentially significant thermospheric GW penetration, effects, and solar cycle influences. The purpose of this paper is to explore these potential influences at greater length with realistic dissipation and thermospheric temperatures.

[7] Our paper is structured as follows. Brief descriptions of the mesoscale convective complex (MCC) and ray trace models are given in section 2. Section 3 examines the effect of increasing background temperature, shear, and dissipation on GW structure and dissipation altitudes. Section 4 describes the GW momentum fluxes and body forces that are created in the thermosphere from a single, deep convective plume during extreme solar minimum and active solar conditions using a canonical wind profile. Section 5 examines the GW momentum fluxes and resulting body forces from the MCC model during extreme solar minimum and active solar conditions. Our conclusions are provided in section 6.

2. Model Formulations

2.1. Mesoscale Convective Complex (MCC) Model

[8] The MCC model used here is identical to that used in VF2004. We briefly review this model here. To represent MCC convection, we generate 30 spatially and temporally localized vertical body forces which simulate convective plumes within the complex. The vertical body forces occur randomly over an hour within a small volume of the tropical

upper troposphere. We do not take into account wind shear effects on the generated GW spectrum within the forcing area [*Beres et al.*, 2002]. The number of plumes is chosen to yield a mesoscale convective pattern similar to *Lane et al.* [2001], with individual plumes having differing diameters, depths, and strengths. (Note, however, that a recent 2-D study suggests a shift in power for the highest-frequency GWs to somewhat smaller horizontal scales and a possible amplitude decrease by one-half when smaller horizontal grid spacings are utilized [*Lane and Knievel*, 2005]). Each plume is Gaussian in the horizontal and vertical directions. The full zonal and meridional widths of each plume, $\mathcal{D}_x$ and $\mathcal{D}_y$, respectively, are equal ($\mathcal{D}_x = \mathcal{D}_y$), and are chosen randomly between 10 and 20 km employing a boxcar probability distribution, $(10 + 10\alpha)$ km, where α is a random number between 0 and 1. The full depth, $\mathcal{D}_z$, is chosen to lie between 3 and 12 km along a probability distribution that emphasizes 3 km over 12 km full depths, $\mathcal{D}_z = (3 + 9\alpha^p)$ km, where p = 2. The amplitude of each vertical body force, w_0, is specified by

$$w_0 = w_1 + (\mathcal{D}_z - \mathcal{D}_{z1})\frac{w_2 - w_1}{\mathcal{D}_{z2} - \mathcal{D}_{z1}}, \tag{1}$$

where $\mathcal{D}_{z1} = 3$ km, $\mathcal{D}_{z2} = 12$ km, $w_1 = 50$ m s^{-1}, and $w_2 = 250$ m s^{-1}. It might be surprising that we are using such large body force amplitudes. However, the 30 vertical body forces yield maximum vertical updraft velocities ranging from 0.1 m s^{-1} to 8.5 m s^{-1}, since a vertical body force is largely balanced by potential temperature and pressure perturbations rather than by large vertical motions. Because convection as represented by linear dynamics may overestimate GW amplitudes by a factor of two as compared to plume updraft velocities [*Song et al.*, 2003], the actual plume updraft velocities associated with the GW spectra outputted from this linear, MCC convection model may be as large as 17 m s^{-1}. Note that updrafts in a strong storm may be as large as 40–50 m s^{-1} [*Cotton and Anthes*, 1989].

[9] Each plume center is chosen randomly to lie within $x_0 = [-50, 50]$ km and $y_0 = [-50, 50]$ km. Because GWs are generated most efficiently when convective plumes impact the stratosphere via penetrative convection, we set the forcing altitude to be $z_0 = z_{tr} - \mathcal{D}_z/2$, where $z_{tr} = 17$ km. The temporal behavior of each plume is cosine squared in time, and the duration of each plume, σ_t, is chosen to be twice the characteristic timescale of the plume based on the Boussinesq dispersion relation. For this MCC, the plume durations range from 13 to 46 min. The starting time for the plumes is randomly chosen to be within $t = [0, 1]$ hour.

[10] Our model calculates the Boussinesq solution in spectral space for each body force at a given time t. Because the solution is linear, the sum of the spectral solutions yields the total spectral solution. The model then takes the inverse Fourier transform of the total spectral solution to determine the solution in real space or calculates the spectral momentum fluxes for the GWs. The averaged, normalized, spectral momentum flux for a GW with wave number $\mathbf{k} = (k, l, m)$ is $\overline{\widetilde{u}\widetilde{w}}\, dk\, dl\, dm$, which has units of m^2 s^{-2} m^3. Here, $\widetilde{u}$ and $\widetilde{w}$ are the analytic solutions for the GW zonal and vertical velocities as calculated in Fourier space from the gravity wave portion of equations (3.13) and (3.15) from *Vadas and Fritts* [2001], and the average is calculated over a wave period. Additionally, $dk = 1/L_x$, $dl = 1/L_y$, and $dm = 1/L_z$ are the spectral grid intervals, where L_x, L_y, and L_z are the total x, y, and z domain lengths of the Boussinesq model. Because we ray trace GWs from each convective plume separately, this model calculates the spectral momentum fluxes separately for each vertical body force after that force has ended.

2.2. Ray Tracing Methodology

[11] Our ray tracing model allows the temperature, wind, density, kinematic viscosity, thermal conductivity, and other background parameters to change as functions of altitude and horizontal location. If a GW with wave number $\mathbf{k} = (k, l, m)$ is propagating in a background wind of $\mathbf{V}(\mathbf{x}) = (V_1, V_2, V_3) = (U, V, 0)$, then the equations that describe its location and refraction are [*Lighthill*, 1978]

$$\frac{dx_i}{dt} = V_i + \frac{\partial \omega_{Ir}}{\partial k_i} = V_i + c_{g_i} \tag{2}$$

$$\frac{dk_i}{dt} = -k_j \frac{\partial V_j}{\partial x_i} - \frac{\partial \omega_{Ir}}{\partial x_i}, \tag{3}$$

where the indices $i, j = 1, 2, 3$ indicate the components of the vector quantities $\mathbf{x}$, $\mathbf{V}$, $\mathbf{k}$, and the group velocity $\mathbf{c}_g = \partial\omega_{Ir}/\partial\mathbf{k}$, repeated indices imply a summation, and ω_{Ir} is the real part of the GW intrinsic frequency: $\omega_{Ir} = \omega_r - kU - lV$, where ω_r is the real part of the ground-based frequency. Here, the intrinsic frequency is defined as $\omega_I = \omega - kU - lV$. The complex anelastic dispersion relation for GWs under the influence of molecular viscosity and thermal diffusivity is (VF2005)

$$(\omega_I - i\alpha\nu)\left(\omega_I - \frac{i\alpha\nu}{\mathrm{Pr}}\right) = \frac{k_H^2 N^2}{\mathbf{k^2} + 1/4H^2}, \tag{4}$$

where $\alpha \equiv -\mathbf{k}^2 + 1/4\mathrm{H}^2 + im/\mathrm{H}$, $\nu = \mu/\overline{\rho}$ is kinematic viscosity, μ is molecular viscosity, $\overline{\rho}$ is density, H is density scale height, Pr is Prandtl number, N is buoyancy frequency, $k_H^2 = k^2 + l^2$, and $\mathbf{k}^2 = k_H^2 + m^2$. Here, an overline denotes the background value which may depend on x, y, and/or z. The usual approach here is to assume a complex vertical or horizontal wave number and real intrinsic frequency [*Pitteway and Hines*, 1963; *Volland*, 1969b; *Francis*, 1973; *Yeh et al.*, 1975; *Hickey and Cole*, 1987]. However, such approaches yield intractable complex equations which must be solved with approximate perturbation expansions, additional assumptions, or numerically. Instead, we take m to be real, and express the intrinsic frequency as a sum of real and imaginary parts: $\omega_I = \omega_{Ir} + i\omega_{Ii}$. Here, ω_{Ir} relates the intrinsic GW frequency to the wave structure, buoyancy frequency, and damping due to kinematic viscosity and thermal diffusivity, and ω_{Ii} expresses the inverse decay rate of the wave amplitude with time due to kinematic viscosity and thermal diffusivity. While the former approach yields altitude-decaying wave amplitudes, the latter approach yields time-decaying wave amplitudes. It can be shown that in the Boussinesq limit, both approaches yield the same dispersion relation and dissipation altitudes (VF2005). The advantage in assuming a complex intrinsic frequency and real vertical wave number is that the complex dispersion relation, equation (4), can be easily solved

separately for ω_{Ii} and ω_{Ir}. This analysis yields the dissipative dispersion relation for a GW in the presence of molecular viscosity and thermal diffusivity:

$$\omega_{Ir}^2 + \frac{\nu^2}{4}\left(\mathbf{k}^2 - \frac{1}{4\mathrm{H}^2}\right)^2\left(1 - \frac{1}{\mathrm{Pr}}\right)^2 \frac{(1 + \delta_+ + \delta^2/\mathrm{Pr})}{(1 + \delta_+/2)^2} + \frac{\nu_+ m\omega_{Ir}}{\mathrm{H}} + \frac{\nu^2 m^2}{\mathrm{Pr}\ \mathrm{H}^2} = \frac{k_H^2 N^2}{\mathbf{k}^2 + 1/4\mathrm{H}^2}, \quad (5)$$

and the inverse GW decay rate with time:

$$\omega_{Ii} = -\frac{\nu}{2}\left(\mathbf{k}^2 - \frac{1}{4\mathrm{H}^2}\right)\frac{[1 + (1 + 2\delta)/\mathrm{Pr}]}{(1 + \delta_+/2)}, \quad (6)$$

respectively, where $\delta = \nu m/\mathrm{H}\omega_{Ir}$, $\delta_+ = \delta\ (1 + \mathrm{Pr}^{-1})$, and $\nu_+ = \nu(1 + \mathrm{Pr}^{-1})$. GW amplitudes and momentum fluxes decay in time as $\exp(-|\omega_{Ii}|t)$ and $\exp(-2|\omega_{Ii}|t)$ because of dissipation, respectively. This dispersion relation is nonhydrostatic and compressible, but excludes acoustic waves similar to *Marks and Eckermann* [1995], and yields the usual anelastic dispersion relation when dissipation is negligible:

$$\omega_{Ir}^2 \simeq \frac{k_H^2 N^2}{m^2 + k_H^2 + 1/4H^2}. \quad (7)$$

Our anelastic formulation is valid as long as $m^2 \gg 1/4\mathrm{H}^2$ or $\lambda_z < 4\pi\mathrm{H}$, where $\lambda_z \equiv 2\pi/|m|$ is the GW vertical wavelength. In deriving equations (4)–(6), the temperature $\overline{T}$, ν, U, V, H, γ, and the sound speed c_s^2 were assumed to vary slowly enough in altitude. In order to quantity how slowly is "slowly" enough, we go back to the equations we solved after implementing the scalings given by equation (17) in VF2005. The vertical distance over which variation occurs for each of these quantities is $[(d\nu/dz)/\nu]^{-1}$, $[(d\overline{T}/dz)/\overline{T}]^{-1}$, $[(dU/dz)/U]^{-1}$, etc. The vertical distance over which the scaled solutions vary is $[(d\widetilde{u}/dz)/\widetilde{u}]^{-1} \simeq m^{-1}$, etc. Thus these quantities vary "slowly" enough when they approximately satisfy

$$\frac{\lambda_z}{2\pi} < \left[\left(\frac{d\nu}{dz}\right)\nu^{-1}\right]^{-1}, \quad \frac{\lambda_z}{2\pi} < \left[\left(\frac{d\overline{T}}{dz}\right)\overline{T}^{-1}\right]^{-1}, \frac{\lambda_z}{2\pi} < \left[\left(\frac{dU}{dz}\right)U^{-1}\right]^{-1}, \quad (8)$$

etc. Note the important factors of 2π in equation (8). Because $[(d\nu/dz)/\nu]^{-1} \sim \mathrm{H}$, a GW must approximately satisfy $\lambda_z < 2\pi\mathrm{H}$ where dissipation becomes important in the thermosphere; this is found to be satisfied for GWs of most importance in the thermosphere (see section 3.2). Additionally, $\lambda_z < 2\pi[(d\overline{T}/dz)/\overline{T}]^{-1}$ is found to be satisfied even in the lower thermosphere under active solar conditions where the temperature gradients are large (see section 3.1). Finally, we find that the solutions appear to be correct even after GWs pass through steep wind shears which do not satisfy equation (8) (see section 3.1).

[12] Our dispersion relation neglects two other forms of dissipation, ion drag and wave-induced diffusion. Ion drag is unimportant during the night for GWs with periods less than a few hours and for GWs with periods less than an hour during the day [*Hines and Hooke*, 1970; *Francis*, 1973; *Hocke and Schlegel*, 1996; *Gossard and Hooke*, 1975]. Wave-induced diffusion occurs because the different molecular species have different scale heights and is important for $z \sim 140$–220 km [*Del Genio and Schubert*, 1979]. For GWs with $\lambda_x = 200$–400 km, this diffusion significantly affects those with periods longer than an hour. The energy densities of upward propagating, shorter-period GWs may be reduced by a factor of two when they reach $z \sim 220$ km; however, insignificant energy density loss occurs above this altitude until kinematic viscosity and thermal conductivity become important.

[13] Since ω_r remains constant along a ray's path provided the unperturbed background variables are independent of time [*Lighthill*, 1978], the intrinsic frequency is determined via $\omega_{Ir} = \omega_r - kU - lV$. The derivatives $\partial\omega_{Ir}/\partial k$, $\partial\omega_{Ir}/\partial l$, $\partial\omega_{Ir}/\partial m$, and $\partial\omega_{Ir}/\partial x_i$ needed for ray tracing are determined from equation (5) and are given by equations (C1)–(C4) in VF2005. The background variables $\overline{T}$, N, H, potential temperature $\overline{\theta}$, pressure $\overline{p}$, $\overline{\rho}$, and $\nu = \mu/\overline{\rho}$ all vary with altitude and the presence of large-scale wave structures. Here, however, we consider only vertical variations of the background temperature. The pressure is determined using the hydrostatic balance equation $d\overline{p}/dz = -g\overline{\rho}$ and the ideal gas law $\overline{p} = R\overline{\rho}\ \overline{T}$:

$$\overline{p}(z) = p_s \exp\left(-\frac{1}{R}\int_0^z \frac{g}{\overline{T}}dz'\right), \quad (9)$$

where g is the acceleration due to gravity, p_s is standard pressure at sea level, $R = k_B/M = 8308/X_{MW}\ \mathrm{m^2\ s^{-2}\ K^{-1}}$, k_B is Boltzmann's constant, and M and X_{MW} are the mass and molecular weight of the particle in the gas, respectively. In addition, $\overline{\rho} = \overline{p}/(R\overline{T})$, $\mathrm{H} = -\overline{\rho}(d\overline{\rho}/dz)^{-1}$, $\overline{\theta} = \overline{T}(p_s/\overline{p})^{R/C_p}$, $N^2 = (g/\overline{\theta})\ d\overline{\theta}/dz$, and $C_p = \gamma\ R/(\gamma - 1)$. Although the average temperature in the lower atmosphere is $\overline{T} \simeq 250$ K, the temperature increases rapidly in the lower thermosphere. During extreme solar minimum, the thermosphere is relatively cold with a temperature of $\overline{T} \simeq 600$ K. During active solar conditions however, the temperature in the thermosphere can be $\overline{T} \simeq 2000$ K [*Banks and Kockarts*, 1973]. Here, we choose five canonical temperature profiles of

$$\overline{T}(z) = \overline{T}_{\max} + (\overline{T}_0 - \overline{T}_{\max})\left[\frac{1}{2}\left(1 - \tanh\left(\frac{z - z_\Delta}{\Delta}\right)\right)\right]^\beta, \quad (10)$$

where $\beta = 0.2$ and $\overline{T}_0 = 246$ K is the background temperature in the deep convection model. Table 1 lists the parameters used to generate the temperature profiles, which are displayed in Figure 1. The temperature profiles II and V are designed to approximate extreme solar minimum and active solar thermospheric temperatures shown by *Banks and Kockarts* [1973]. Temperature profiles III and IV are interpolations. These profiles can also approximate differing daytime temperature profiles, although care must be taken since ion drag is neglected here. The isothermal profile (I) is included for comparison with VF2004 and VF2005 and

Table 1. Temperature Profiles

Number	$\overline{T}_{\max}$, K	$z\Delta$, km	Δ, km
I	246	—	—
II	600	104	13.0
III	1000	112	16.0
IV	1500	120	19.8
V	2000	126	23.5

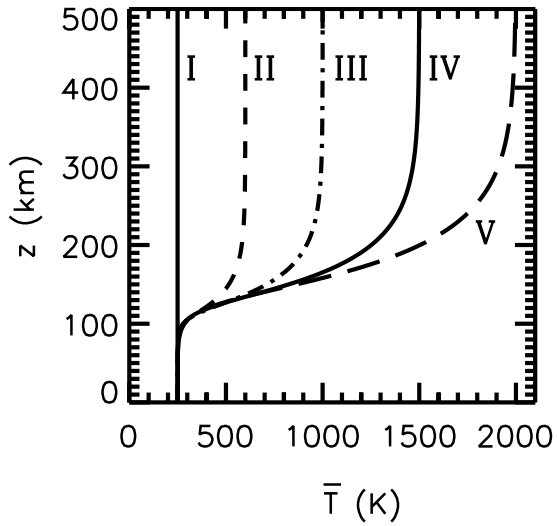

Figure 1. Model thermospheric temperature profiles used in this paper. The solid line denotes an isothermal atmosphere (profile I). The dash, dash-dot, dash-dot-dot-dot, and long dash lines show our models for extreme solar minimum through active solar conditions as profiles II, III, IV, and V, respectively, as labeled.

for normalization of the spectral momentum fluxes in section 4.1.

[14] In our ray trace model we set $\mu = 0.017$ gm m^{-1} s^{-1}, which yields a kinematic viscosity at 90 km of $\nu = \mu/\overline{\rho} = 6.5$ m^{2}s^{-1}, similar to the value used by *Pitteway and Hines* [1963]. We also set Pr = 0.7, characteristic of the value in the mesosphere and lower thermosphere [*Kundu*, 1990], and thus ignore its slight variations with temperature [*Yeh et al.*, 1975]. Additionally, we set $\gamma = 1.4$ and $X_{MW} = 30$, although γ increases and X_{MW} decreases somewhat in the thermosphere because of the changing gas components [*Midgley and Liemohn*, 1966; *Francis*, 1973]. We allow initially downward propagating waves to reflect upward at $z = 0$. All other GWs that reflect at $z = 0$ are eliminated. We also eliminate GWs with vertical wavelengths of $\lambda_z > 0.95$ $(4\pi \mathrm{H}(z))$ when ray tracing GWs from single and multiple plumes in order to ensure that our results are valid within the anelastic approximation. In the lower atmosphere, H $\simeq$ 7 km, so GWs with $\lambda_z > 84$ km are removed from the GW spectrum above the lower atmospheric shear. We show in section 3 that most of the GWs that satisfy the anelastic assumption in the lower atmosphere will increasingly satisfy the anelastic assumption in the thermosphere where the temperatures are much larger. Exceptions are GWs with frequencies nearly equal to the thermospheric buoyancy frequencies.

[15] To achieve accurate numerical solutions, a fourth-order Runge Kutta routine [*Press et al.*, 1992] is employed to advance the ray equations in time. The time step is kept small enough so that the variables change less than 25% each time step, and the GW is not allowed to travel more than 0.25 km/$|c_{g_z}|$ each time step. In addition, there is a minimum time step of 1.0×10^{-8} km/$|c_{g_z}|$ in order to keep last-digit errors from accumulating. Wave saturation effects are not included here, since the GWs that dissipate well within the thermosphere have sufficiently small amplitudes and large phase speeds below the turbopause to likely avoid saturation.

3. Gravity Wave Structure and Dissipation in the Thermosphere

[16] In a previous paper, VF2005 explored how dissipation affects GW structure in an isothermal atmosphere with $\overline{T} \simeq 250$ K. Since the thermosphere is much hotter than the lower atmosphere because of solar heating, it is important to explore GW structure changes in a realistic thermospheric environment. Therefore we investigate how GW structure changes and dissipation altitudes depend on background temperatures, wind shears, and dissipation.

3.1. Gravity Wave Structure Changes From Increasing Temperatures

[17] In order to isolate the effect that increasing background temperature has on a GW's structure as it propagates upward in the thermosphere, we first ray trace GWs in an atmosphere with zero dissipation and zero wind shear for varying thermospheric temperatures. Figure 2 shows with solid contours the vertical wavelengths of GWs after they have propagated upwards through the changing temperature environment (i.e., at the top of the z-domain, remembering that dissipation is assumed to be zero here) as a function of the horizontal and initial vertical wavelengths. As expected, a GW's vertical wavelength in the thermosphere is larger than in the lower atmosphere, and this increase is much larger when the Sun is active than when the Sun is quiet [*Richmond*, 1978]. Additionally, very high frequency GWs reflect downwards because of evanescence when $\omega_{Ir} = N(z)$ (gray shading). Note that the gray-shaded region increases as the temperature in the thermosphere increases. The reflection and ducting of GWs near the base of the thermosphere where the temperature rises steeply has been studied previously [*Pitteway and Hines*, 1965; *Midgley and Liemohn*, 1966; *Hocke and Schlegel*, 1996].

[18] We now derive an expression for λ_z which depends on the thermosphere's larger temperature, as well as on background winds. This expression will allow for an enhanced understanding of the role $\overline{T}$ plays in changing a GW's vertical wavelength and will allow for validation of our ray trace model. As the asymptotic temperature in the thermosphere increases, the asymptotic Boussinesq frequency decreases, as can be seen by the constant temperature (isothermal) expressions:

$$N^2 \simeq g^2 \frac{(\gamma - 1)}{\gamma R \overline{T}} = \frac{g(\gamma - 1)}{\gamma \mathrm{H}} \tag{11}$$

$$\mathrm{H} \simeq R\overline{T}/g. \tag{12}$$

These expressions can be derived from equation (9) and the equations following it assuming constant $\overline{T}$. Here, asymptotic refers to the region in the thermosphere that is approximately isothermal (e.g., $z > 200$–300 km (see Figure 1)). Because $U = V = 0$ in Figure 2, the intrinsic frequency is constant, and because there are no horizontal background variations, k_H^2 is also constant (see equation (3)). If an upward propagating GW has an intrinsic frequency that is larger than the buoyancy frequency in the thermosphere, it will reflect back downward.

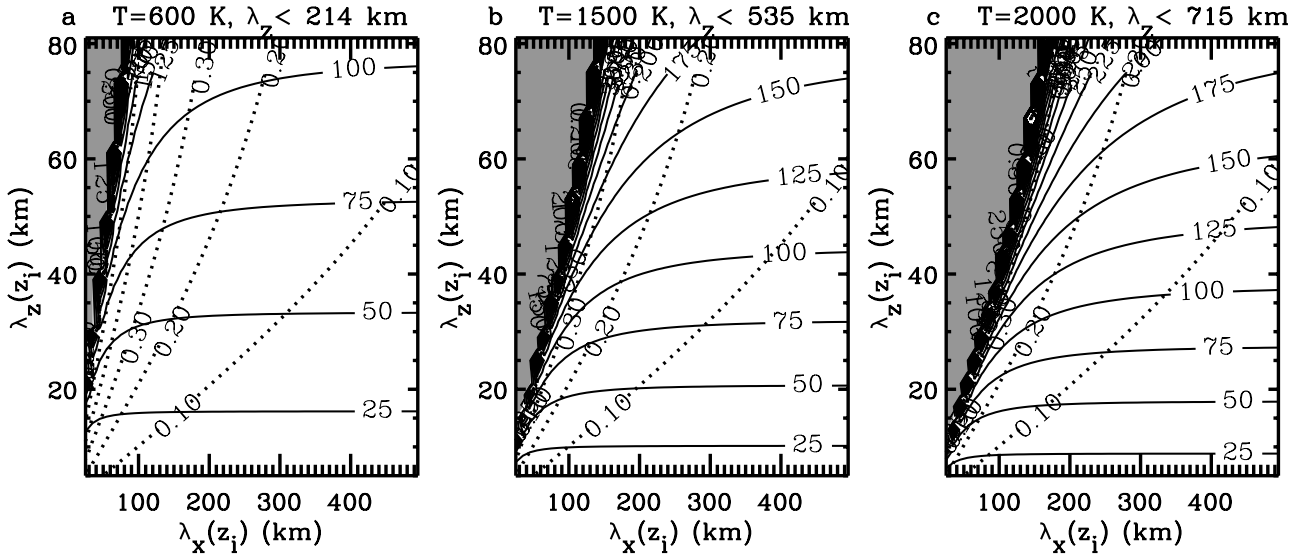

Figure 2. Vertical wavelengths for GWs in the thermosphere with zero dissipation and zero wind shear (solid lines) in 25 km intervals as a function of the initial GW horizontal and vertical wavelengths in the lower atmosphere. (a) $\overline{T}_{\max}$ = 600 K (profile II); (b) $\overline{T}_{\max}$ = 1500 K (profile IV); (c) $\overline{T}_{\max}$ = 2000 K (profile V). Dotted lines show the initial GW intrinsic frequencies divided by $N_0 = 0.02$ s^{-1} in intervals of 0.1. Gray shading depicts those GWs which reflect back downward because of evanescence due to increasing $\overline{T}$ and decreasing N. The label for each plot includes the asymptotic temperature and the limit on λ_z for which the anelastic approximation is valid.

For GWs with frequencies much smaller than the buoyancy frequency in the thermosphere, $m^2 \gg k_H^2 + 1/4\mathrm{H}^2$, so that a GW's vertical wavelength increases as the buoyancy frequency decreases, $\lambda_z \propto N^{-1}$, from equation (7). Using equation (11), λ_z increases as the square root of the background temperature when dissipation is unimportant for lower-frequency GWs:

$$\lambda_z(z) \simeq \lambda_z(z_i)\sqrt{\overline{T}/\overline{T}_0}, \tag{13}$$

where z_i is the altitude in the lower atmosphere where the GW is generated, or more generally, the altitude just below where the temperature begins to increase. Although equation (13) holds for lower-frequency GWs with $\omega_{Ir} \ll N$, λ_z increases by much more than $\sqrt{\overline{T}/\overline{T}_0}$ for GWs with frequencies near the smaller thermospheric buoyancy frequency. We include this important effect for high-frequency GWs as well as shear effects in the lower atmosphere and thermosphere. Using

$$N^2 = N_0^2\overline{T}_0/\overline{T} \tag{14}$$

$$\mathrm{H} = \mathrm{H}_0\overline{T}/\overline{T}_0, \tag{15}$$

obtained from equations (11)–(12), where the subscript "0" denotes the average value in the lower atmosphere, rearrangement of equation (7) yields

$$m_i^2 = k_H^2\left(\frac{N_0^2}{\omega_r^2} - 1\right) - \frac{1}{4\mathrm{H}_0^2}, \tag{16}$$

$$m^2 = k_H^2\left(\frac{\overline{T}_0 N_0^2}{\overline{T}(\omega_r - kU - lV)^2} - 1\right) - \frac{\overline{T}_0^2}{4\mathrm{H}_0^2\overline{T}^2}, \tag{17}$$

where $m_i = m(z_i)$. Equation (16) is the dispersion relation for a GW in the initial source spectrum (in the intrinsic frame of reference), while equation (17) is the dispersion relation for a GW in the asymptotic region of the thermosphere with an intervening shear, ignoring dissipation. Solving equations (16)–(17), a GW's vertical wavelength in the asymptotic region of the thermosphere, again ignoring dissipation, is given by

$$\lambda_z = \lambda_z(z_i)\sqrt{\frac{\overline{T}}{\overline{T}_0}}\left[\psi - \left(\frac{\overline{T}}{\overline{T}_0} - \psi\right)\frac{k_H^2}{m_i^2} - \left(\frac{\overline{T}_0}{\overline{T}} - \psi\right)\frac{1}{4\mathrm{H}_0^2 m_i^2}\right]^{-1/2}, \tag{18}$$

where

$$\psi \equiv \frac{\omega_r^2}{(\omega_r - kU - lV)^2}. \tag{19}$$

For high-frequency GWs then, the dependence of λ_z on the background temperature is more complicated than equation (13). Plots of equation (18) (not shown) look virtually identical to Figure 2, thereby validating our ray trace model in the presence of temperature gradients but in the absence of wind shear and dissipation.

[19] Although a GW's vertical wavelength is larger in the thermosphere than in the lower atmosphere, the anelastic approximation is increasingly satisfied in the thermosphere for most GWs. This is because the right-hand side of the anelastic criterion, $\lambda_z < 4\pi\mathrm{H} = 4\pi\mathrm{H}_0\overline{T}/\overline{T}_0$ (using equation (15)), increases more rapidly with altitude than the slower increase of λ_z with altitude, $\lambda_z \simeq \lambda_z(z_i)\sqrt{\overline{T}/\overline{T}_0}$. For example, GWs in the lower atmosphere with λ_x = 400 km and λ_z = 75 km just satisfy the anelastic approximation requiring $\lambda_z < 88$ km. During active solar conditions with $\overline{T}$ = 2000 K, λ_z increases substantially to 175 km

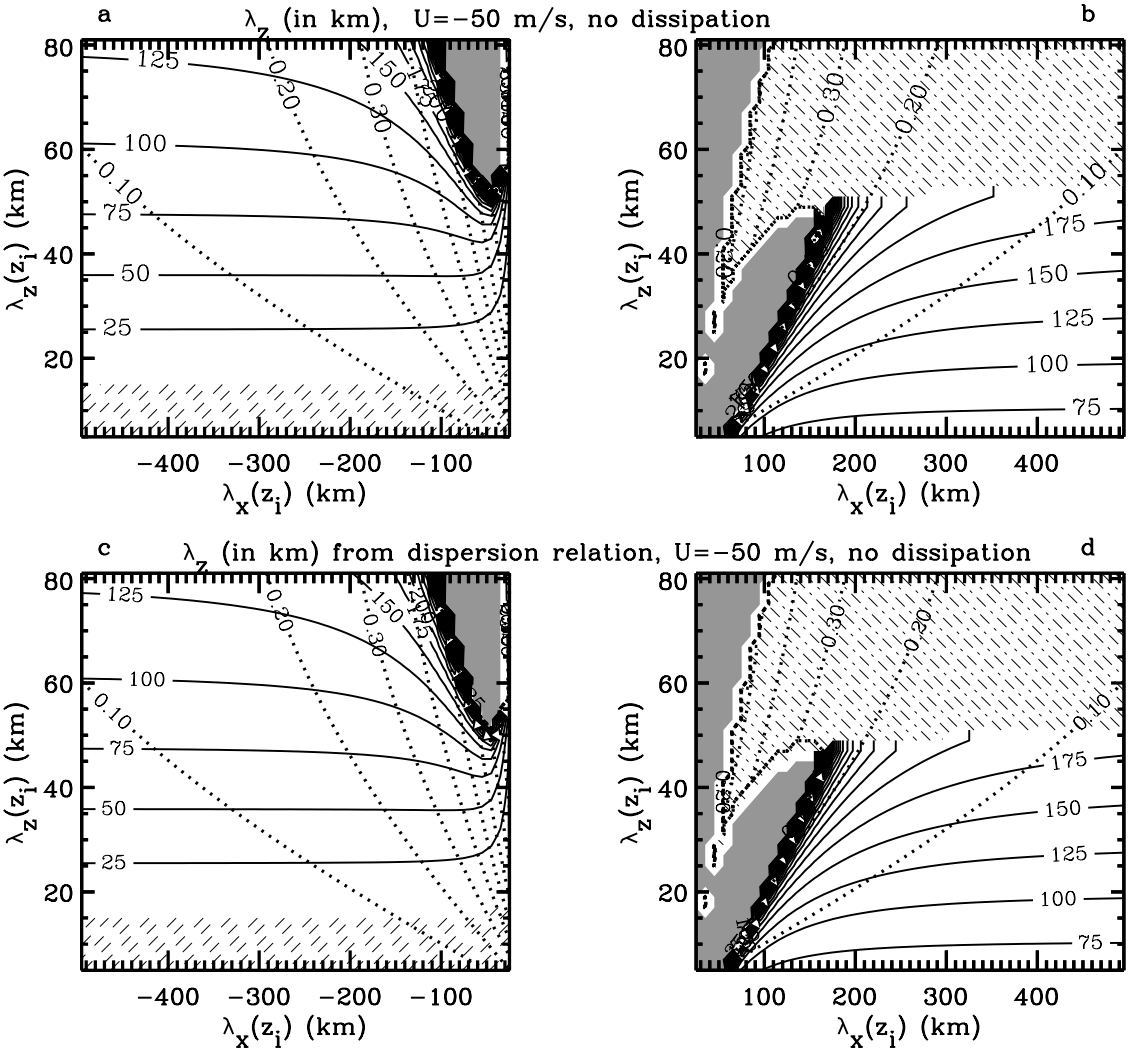

Figure 3. Vertical wavelengths for GWs in the thermosphere with $\overline{T}_{max}$ = 2000 K (profile V) with zero dissipation and a shear of $\overline{U}$ = 50 m s^{-1} (solid lines) in 25 km intervals as a function of the initial GW horizontal and vertical wavelengths. (a) Westward propagating GWs from the ray trace model; (b) Eastward propagating GWs from the ray trace model; (c) Westward propagating GWs from the dispersion relation given by equation (18); (d) Eastward propagating GWs from the dispersion relation given by equation (18). Dotted lines and gray shading are the same as in Figure 2. Hatched areas in the upper portions of Figures 3b and 3d are GWs that were removed from the spectrum because they violated the anelastic approximation, $\lambda_z < 4\pi H$. Hatched areas in the lower portions of Figures 3a and 3c are GWs that were removed from the spectrum after encountering critical levels.

in the absence of dissipation and shear (see Figure 2c). However, the anelastic criterion in this thermosphere is $\lambda_z <$ 715 km, which is easily satisfied.

[20] Because shear is nearly always present in the lower atmosphere and thermosphere through the presence of large-scale waves and tides, as well as solar and electrodynamic effects [e.g., *Larsen*, 2002; *Larsen et al.*, 2003], we include shear here in order to understand its role in altering GW structure as observed within the hotter thermosphere. We choose the wind in our model to be zonal ($V = 0$) with shear in the lower atmosphere:

$$U(z) = \frac{1}{2}\overline{U}[1 - \tanh((z - z_d)/\Delta)]. \quad (20)$$

Here, z_d = 30 km, and Δ = 5 km. In Figures 3a–3b, we show λ_z for GWs ray traced under active solar conditions ($\overline{T}$ = 2000 K) after propagating out of the shear given by equation (20) with $\overline{U}$ = 50 m s^{-1}. The hatched region in the upper portion of Figure 3b denotes GWs excluded by the anelastic criterion, while the hatched region in the lower portion of Figure 3a denotes GWs eliminated by critical levels (i.e., $\omega_r - kU - lV \simeq 0$). As expected, the GW spectrum is anisotropic after propagating through this shear, with an increase in λ_z and ω_{Ir} for eastward propagating GWs, and a decrease in λ_z and ω_{Ir} (and critical level removal) for westward propagating GWs [*Hines and Reddy*, 1967].

[21] Figures 3c–3d shows λ_z obtained from the theoretical expression equation (18). Comparing with Figures 3a–3b,

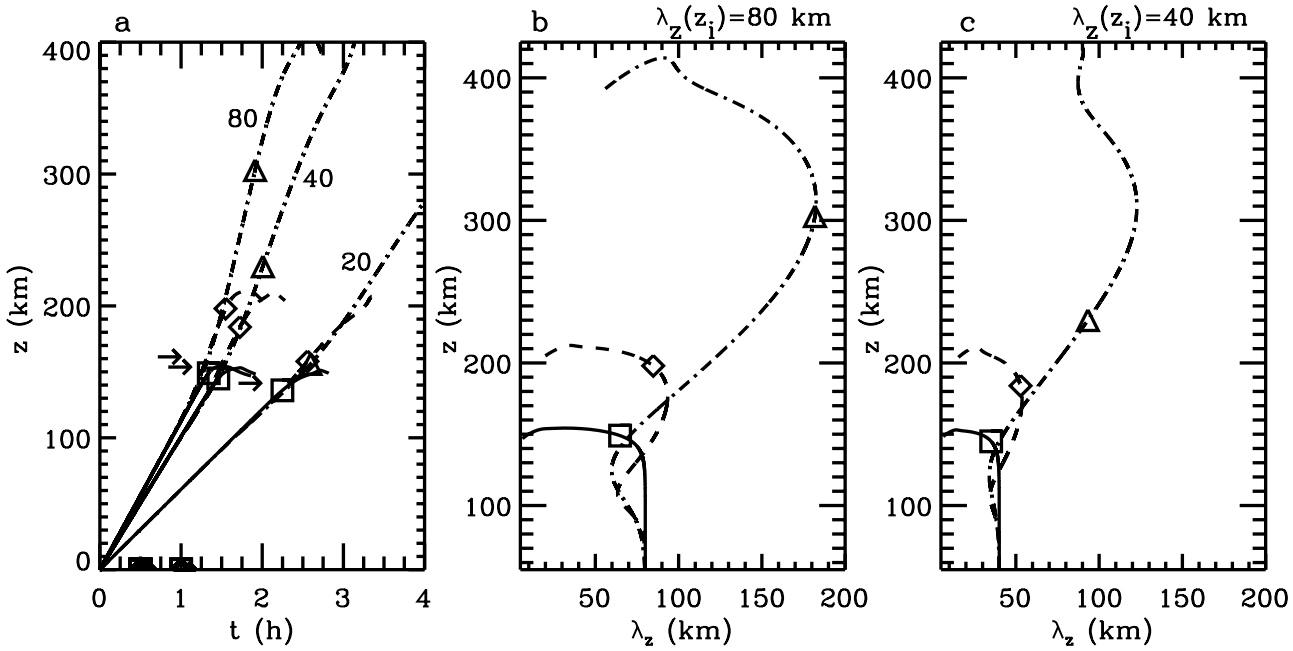

Figure 4. (a) The ray paths for three high-frequency GWs that are initially located at $z = z_i = t = 0$. The solid, dash, and dash-dot lines are for GWs propagating from the lower atmosphere into the thermosphere using temperature profiles I, II, and V, respectively. These GWs have $l = 0$ and are initially propagating upwards in a zero wind environment. Ray paths are labeled by λ_z (in kilometers). The boxes, diamonds, and triangles show the altitudes and times where the GW momentum fluxes are maximum (i.e., z_{diss}) for profiles I, II, and V, respectively. The arrows show the estimated dissipation altitudes in an isothermal, Pr = 1 atmosphere using equation (26) with the assumption that m is constant with altitude. (b) Vertical wavelength as a function of altitude for the $\lambda_z(z_i) = 80$ km GWs shown in a) with the same line types and symbols. (c) Vertical wavelength as a function of altitude for the $\lambda_z(z_i) = 40$ km GWs shown in Figure 4a with the same line types and symbols.

we see that the ray trace code accurately calculates the correct GW structure that results from the wind and temperature gradients. Using equation (8), we check to see if our "slowly varying" approximations are valid for large λ_z GWs. The smallest value of $2\pi[(d\overline{T}/dz)/\overline{T})]^{-1}$ for this (active solar) temperature profile is ~230 km at $z \sim 130$ km, which is larger than nearly all of the asymptotic thermospheric values of λ_z shown in Figures 2–3. Therefore we conclude that the condition $\lambda_z < 2\pi[(d\overline{T}/dz)/\overline{T})]^{-1}$ is approximately satisfied, even during active solar conditions and in the lower thermosphere where the temperature gradients are large. The condition for $U(z)$ from equation (8), however, is not as well satisfied. Because we chose a steep velocity profile, equation (20), the value of $2\pi\ [(dU/dz)/U)]^{-1}$ is ~16 km at $z = 0$–20 km and is 30 km at $z \simeq 30$ km. These scale heights are small compared to many of the lower atmospheric $\lambda_z(z_i)$ values depicted in Figure 3. Because of this, we would have expected the ray trace results for large λ_z to be spurious in the thermosphere because of errors made in calculating m in the lower atmosphere as the GWs passed through the shear region. However, comparison of Figures 3a–3b with Figures 3c–3d show no such errors for GWs with $\lambda_z(z_i) > 16$ km. Therefore we conclude that the ray trace equations appear to give the correct results even when $\lambda_z > 2\pi\ [(dU/dz)/U)]^{-1}$.

3.2. Gravity Wave Structure Changes With Dissipation

[22] In the previous section we noted that a GW's vertical wavelength increases substantially with increasing temperature in the absence of dissipation, with equation (18) representing the maximum possible vertical wavelength obtainable in the thermosphere. If we include the effects of dissipation, however, this increase is smaller because a GW typically dissipates at altitudes where the temperature is smaller than the asymptotic temperature.

[23] We examine the effect dissipation has on GW structure by ray tracing three high-frequency GWs with similar frequencies and differing wavelengths into the thermosphere. The initial wavelength pairs (λ_x, λ_z) in kilometers are (240, 80), (120, 40), and (60, 20), where $\lambda_x \equiv 2\pi/|k|$ and $\lambda_z \equiv 2\pi/|m|$. The resulting ray paths as a function of time (in hours) are shown in Figure 4a as solid, dash, and dash-dot lines for the corresponding temperature profiles I, II, and V, respectively. Ray paths are labeled by λ_z (in kilometers). The boxes, diamonds, and triangles show the dissipation altitudes, z_{diss}, for temperature profiles I, II, and V, respectively. Here, the dissipation altitude z_{diss} is defined as the altitude where the GW momentum flux (per unit mass) is maximum. As the temperature in the thermosphere increases, GWs propagate to increasingly higher altitudes before dissipating [*Pitteway and Hines*, 1963; *Francis*, 1973; *Yeh et al.*, 1975; *Richmond*, 1978; *Cole and Hickey*,

1981]. GWs with the largest initial vertical wavelengths are most affected by increasing thermospheric temperatures and dissipate at the highest altitudes. The larger slope above $z \sim 150$ km indicates increased vertical group velocities, and larger vertical wavelengths and frequencies [*Richmond*, 1978]. In contrast, GWs with the smallest initial vertical wavelengths are least affected by thermospheric temperatures and dissipate at altitudes which do not depend very sensitively on the asymptotic thermospheric temperature. This is because the temperature profiles in the lower thermosphere for $z < 150$ km are nearly the same here (see Figure 1). The GWs with $\lambda_z(z_i) = 80$ km dissipate at $z \simeq 150$, 200, and 305 km in temperature profiles I, II and V, respectively, while the GWs with $\lambda_z(z_i) = 40$ km dissipate much lower at altitudes of $z \simeq 145$, 185, and 230 km in temperature profiles I, II, and V, respectively. Thus GW vertical wavelengths increase in the thermosphere due to two distinct effects, the first being the increase in λ_z of individual GWs because of the increasing background temperature and the second being the dissipative filtering of GW spectra by vertical wavelength. GW vertical wavelengths have been observed to increase with altitude in the thermosphere [*Oliver et al.*, 1997; *Djuth et al.*, 1997]. Note that the dissipative filtering of GWs via vertical wavelength and frequency was found previously using differing dissipative models [*Pitteway and Hines*, 1963; *Volland*, 1969b].

[24] We now derive the quenching criterion of a GW from dissipation. The momentum flux of a GW (prior to dissipating) is maximum when (equation (54) of VF2005)

$$2\omega_{Ii}\mathrm{H}/c_{gz} \simeq -1. \tag{21}$$

This expression relates the intrinsic properties of a GW to the background structure and kinematic viscosity at the dissipation altitude and states that a GW dissipates when the dissipative decay time equals the time taken for the GW to propagate two density scale heights in altitude. Although it was derived in an isothermal atmosphere with $\lambda_z < \mathrm{H}$, it will be shown to replicate the ray trace results in realistic temperature profiles very well, even for GWs with very large λ_z and for GWs which dissipate in the lower thermosphere where the temperature gradient is large. Since the Prandtl number is close to 1 in the Earth's atmosphere, and the equations simplify considerably when Pr = 1, we set Pr = 1 in equation (6) of this paper and in equation (C3) of VF2005. For anelastic GWs with $\lambda_z < 4\pi\mathrm{H}$ in an arbitrary temperature profile then, the inverse decay rate is $\omega_{Ii} \simeq -\nu(\mathbf{k}^2 - 1/4\mathrm{H}^2)$ and the vertical group velocity is

$$c_{g_z} = \frac{\partial\omega_{Ir}}{\partial m} \simeq \frac{-m|k_H|N}{\left(\mathbf{k}^2 + 1/4\mathrm{H}^2\right)^{3/2}} - \frac{\nu}{\mathrm{H}}. \tag{22}$$

Using equation (21), the quenching criterion of a GW from dissipation then is

$$\nu_{\mathrm{diss}} \simeq \frac{|k_H m|N}{2\mathrm{H}\left(\mathbf{k}^2 + 1/4\mathrm{H}^2\right)^{5/2}}. \tag{23}$$

Equation (23) can be solved iteratively for the absolute value of the vertical wave number $m_a = 2\pi/\lambda_z$ as

$$m_a = \sqrt{\left(\frac{k_H N}{2\mathrm{H}\nu}\right)^{2/5} m_a^{2/5} - k_H^2 - \frac{1}{4\mathrm{H}^2}}, \tag{24}$$

where the first guess for m_a on the right-hand side (RHS) of equation (24) is

$$m_a = \sqrt{\sqrt{\frac{k_H N}{2\mathrm{H}\nu}} - k_H^2 - \frac{1}{4\mathrm{H}^2}}, \tag{25}$$

and the second guess for m_a on the RHS of equation (24) is the value of m_a determined on the left-hand side of equation (24) from the first iteration. This procedure is iterated until convergence in m_a is obtained.

[25] For the special case of an isothermal temperature profile, ν increases exponentially with altitude as $\nu = \nu_1 \exp((z - z_1)/\mathrm{H})$, yielding an approximate dissipation altitude from equation (23) of

$$z_{\mathrm{diss}} \simeq z_1 + \mathrm{H}\ln\left(\frac{|k_H m|N}{2\mathrm{H}\left(\mathbf{k}^2 + 1/4\mathrm{H}^2\right)^{5/2}\nu_1}\right), \tag{26}$$

where $\nu_1 = \nu(z_1)$, and z_1 is an altitude well below the dissipation altitude. For medium frequency waves where $\mathbf{k}^2 + 1/4\mathrm{H}^2 \simeq m^2$, this becomes $z_{\mathrm{diss}} \simeq z_1 + \mathrm{H}\ln(\omega_{Ir}/2\mathrm{H}|m|^3\nu_1)$, which is equation (73) from VF2005. This shows that the atmosphere is a vertical wavelength- and frequency-dependent selective filter, as noted previously [*Volland*, 1969a]. We plot values of equation (26) as arrows in Figure 4a with $z_1 = z_i = 0$, and approximate m to be the vertical wave number at $z = t = 0$ for simplicity, even though $|m|$ decreases with altitude. The estimated dissipation altitudes slightly overestimate the actual dissipation altitudes for temperature profile I when λ_z is large because the assumption that $|m|$ is constant with altitude is not well satisfied.

[26] In Figures 4b and 4c, we show λ_z for $\lambda_z(z_i) = 80$ km and $\lambda_z(z_i) = 40$ km, respectively. We see that λ_z decreases somewhat in the lower thermosphere because of the small increase of the buoyancy frequency that arises from the sudden and rapid increase in temperature. Then, when the temperature increases more uniformly, N decreases (see equation (14)), and λ_z increases in the thermosphere, especially during active solar conditions (see section 3.1). When dissipation becomes important, λ_z decreases rapidly, as discussed previously (VF2005), and as found numerically [*Zhang and Yi*, 2002]. This is in contrast to the Boussinesq theoretical result (VF2005) and perturbation expansion theory results [*Pitteway and Hines*, 1963; *Hines*, 1968], for which λ_z increases as a GW with $\lambda_z < \mathrm{H}$ dissipates.

[27] We now check the validity of the ray trace solutions to ensure that ν changes slowly enough as these GWs dissipate. The values of $2\pi\ [(d\nu/dz)/\nu]^{-1} \sim 2\pi\mathrm{H}$ for the $\lambda_z(z_i) = 80$ km GWs shown in Figure 4b at the dissipation altitudes are ~105 km and ~350 km for temperature profiles II and V, respectively. The corresponding vertical wavelengths at z_{diss} are $\lambda_z \sim 80$ km and 180 km, respectively, which shows that for this GW, ν changes slowly enough. For the $\lambda_z(z_i) = 40$ km GWs shown in Figure 4c, $2\pi[(d\nu/dz)/\nu]^{-1} \sim 90$ km and 305 km for temperature

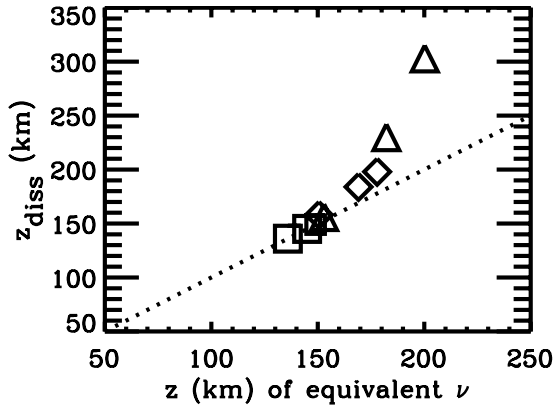

Figure 5. The dissipation altitudes, z_{diss}, for the GWs shown in Figure 4a (using the same symbols) as a function of the altitude of equivalent kinematic viscosity ν. The dot line guides the eye by showing the altitudes of equivalent ν.

profiles II and V, respectively. The corresponding vertical wavelengths at z_{diss} are $\lambda_z \simeq 50$ km and 95 km, respectively, which again shows that for this GW, ν changes slowly enough. Therefore the condition $\lambda_z < 2\pi[(d\nu/dz)/\nu]^{-1}$ from equation (8) is well satisfied for typical GWs of most importance in the thermosphere (see section 4). Note that the condition is better satisfied for these GWs during active solar conditions when the density scale height is large than during extreme solar minimum.

[28] Strong dissipation may cause a GW to partially reflect downward as it continues to propagate upward while dissipating [*Midgley and Liemohn*, 1966; *Yanowitch*, 1967; *Volland*, 1969b]. When this occurs, a GW can no longer be represented by a single upgoing or downgoing wave, and ray theory breaks down. This can be diagnosed along a ray path by calculating the residue [*Einaudi and Hines*, 1970; VF2005]. Here, we assume that all ray paths are valid until well after a GW dissipates, at which point ray theory may break down with little overall effect on the GW momentum flux profile. This assumption is shown to be valid for GWs originating in the lower atmosphere which satisfy the anelastic condition that $\lambda_z \leq 4\pi$H (S. L. Vadas, Horizontal and vertical propagation, and dissipation of gravity waves in the thermosphere from lower atmospheric and thermospheric sources, submitted to *Journal of Geophysical Research*, 2006, hereinafter referred to as Vadas, submitted manuscript, 2006); detailed residue calculations and implications are discussed by Vadas (submitted manuscript, 2006) for lower atmospheric and thermospheric sources of GWs.

[29] In Figure 5, we display the dissipation altitudes, z_{diss}, for the GWs shown in Figure 4a as a function of the altitude of equivalent kinematic viscosity ν. The altitude of equivalent kinematic viscosity ν is computed by determining ν at the actual dissipation altitude for a GW in an isothermal atmosphere, and then computing the altitude where ν is the same in another temperature profile. For GWs with $\lambda_z(z_i) \leq$ 40 km, the dissipation altitudes can be estimated fairly well using the equivalent ν altitude. However, for the GWs with $\lambda_z(z_i)$ = 80 km, the equivalent ν altitude substantially underestimates the actual dissipation altitudes by 50–100 km. This is because λ_z increases substantially prior to dissipation for these GWs, thereby enabling much higher penetration and dissipation altitudes.

[30] In Figures 6a, 6b, and 6c, we show some of the fundamental results of this new anelastic GW dispersion relation. The initial, lower atmospheric GW vertical wavelengths are shown on the y-axis, while the maximum thermospheric GW vertical wavelengths are shown as solid

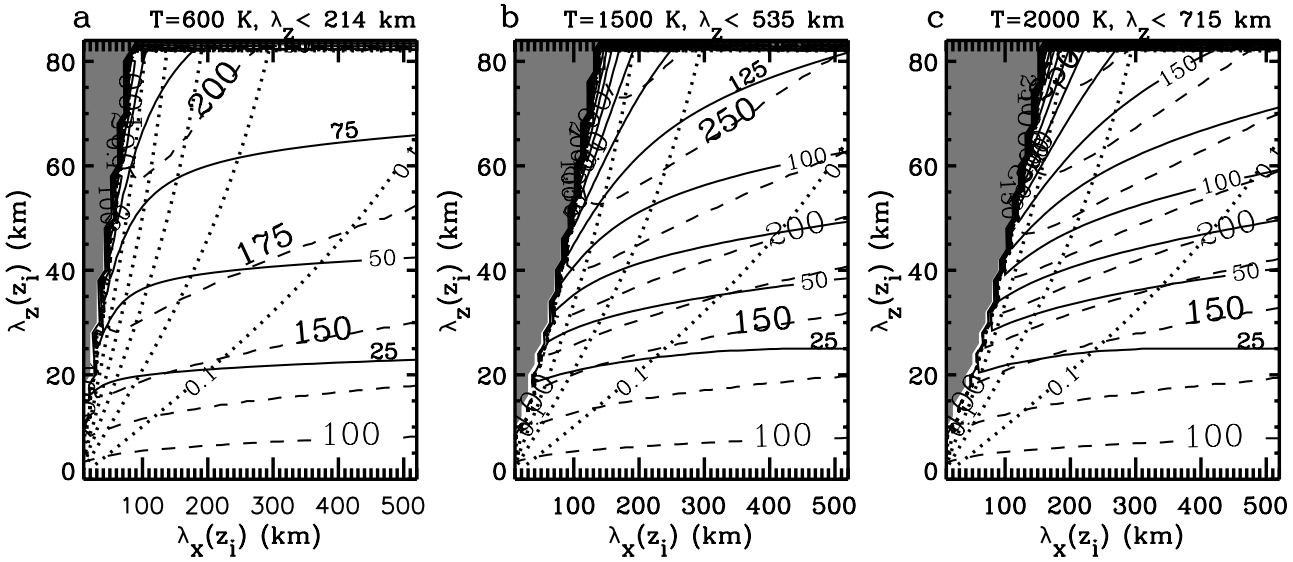

Figure 6. Maximum GW vertical wavelengths below the dissipation altitude in a thermosphere with dissipation but with no shear (solid lines, labeled with small numbers) in 25 km intervals, as a function of the initial GW horizontal and vertical wavelengths in the lower atmosphere. (a) $\overline{T}_{max}$ = 600 K (profile II); (b) $\overline{T}_{max}$ = 1500 K (profile IV); (c) $\overline{T}_{max}$ = 2000 K (profile V). Dash lines (labeled by large numbers) show the dissipation altitudes in 25 km intervals. Dotted lines (only "0.1" is labeled) and gray shading are the same as in Figure 2.

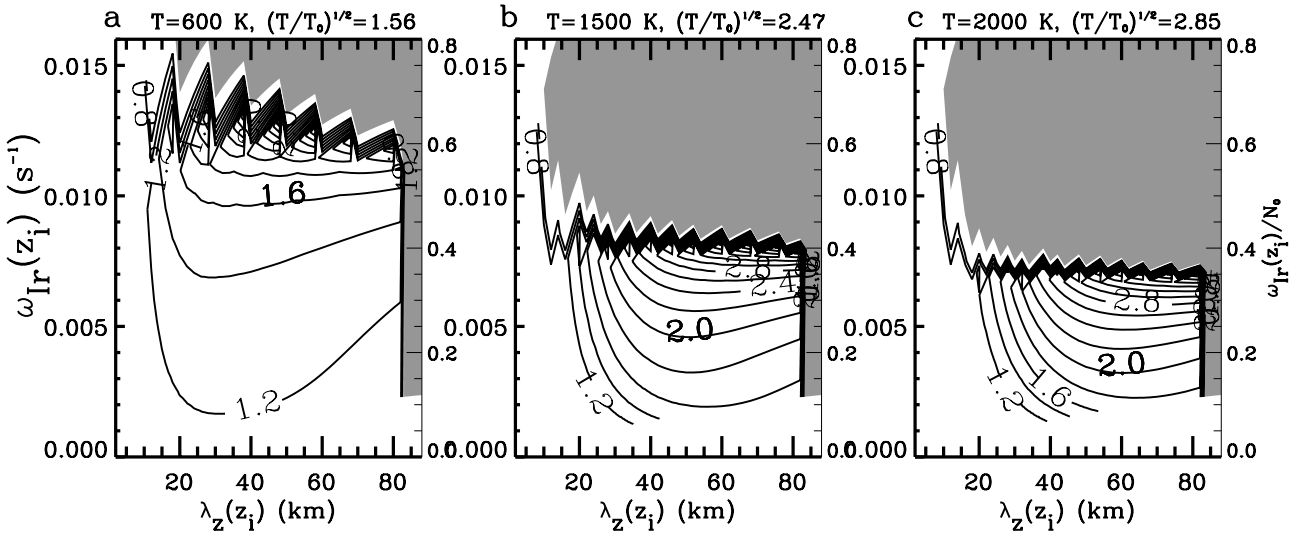

Figure 7. Maximum GW vertical wavelengths (as in Figure 6) divided by $\lambda_z(z_i)$ (solid lines) in intervals of 0.2, as a function of the initial GW vertical wavelength and intrinsic frequency. (a) $\overline{T}_{\max}$ = 600 K (profile II); (b) $\overline{T}_{\max}$ = 1500 K (profile IV); (c) $\overline{T}_{\max}$ = 2000 K (profile V). The right-hand y-axis displays $\omega_{Ir}(z_i)/N_0$. Gray shading is the same as in Figure 2. The label for each plot includes the asymptotic temperature and $\sqrt{\overline{T}_{\max}/\overline{T}_0}$. The jagged boundary at $\omega_{Ir}(z_i) \simeq N$ is an artifact of the finite number of GWs ray traced and the interpolation scheme for the contour plot (i.e., no smoothing was used to preserve the sharp boundaries).

contours. As before, the maximum vertical wavelengths in the thermosphere are significantly larger than in the lower atmosphere for GWs with initially large λ_z, especially during active solar conditions. The maximum vertical wavelength for GWs with initially small λ_z do not increase by as much because these GWs dissipate in the lower thermosphere where the temperatures are not very much larger than in the lower atmosphere. Thus Figure 6 essentially shows the range of allowed λ_z for a GW in the thermosphere given a horizontal wavelength λ_x and intrinsic frequency (excepting the slight decrease in λ_z that occurs in the lower thermosphere (see Figures 4b–4c)). For example, for a GW with λ_x = 400 km and ω_{Ir}/N_0 = 0.1 (which has a period of 50 min since $N_0 = 0.02$ s^{-1}), the range of allowed λ_z is ~45–75 km for temperature profile IV. We also show the dissipation altitudes (dash lines). The dissipation altitudes increase as λ_z (z_i) increases, and for a given λ_z (z_i), the dissipation altitudes decrease as λ_x increases due to the decreasing intrinsic frequency. We also show in Figure 6 those GWs which experience evanescence (gray shading). Note that the region of evanescence is similar to that in Figure 2, showing that these GWs reflect as described previously before succumbing to dissipation. Although these very high frequency GWs may not contribute to the body force in the thermosphere, they may still be candidates for seeding Rayleigh-Taylor instabilities, equatorial spread F (ESF), and plasma bubbles prior to reflecting [e.g., *Kelley*, 1989]. During extreme solar minimum, Figure 6 shows that the maximum dissipation altitudes and vertical wavelengths are $z_{\rm diss} \sim 225$ km and $\lambda_z \sim 75$–150 km, while for active solar conditions with $\overline{T}_{\max}$ = 2000 K, the maximum dissipation altitudes and vertical wavelengths are $z_{\rm diss} \sim$ 275–325 km and $\lambda_z \sim 150$–250 km. These maximum values are achieved for GWs with $\lambda_x \sim 50$–300 km and $\lambda_z(z_i) \sim 50$–85 km. Further calculations involving this dispersion relation are given by Vadas (submitted manuscript, 2006).

[31] We compare our results with *Djuth et al.* [1997], who observed vertical half wavelengths over Arecibo of 2–25 km between 115 and 160 km altitudes. We assume that lower atmospheric GW spectra are dominated by vertical wavelengths of $\lambda_z \sim$10 km, with decreasing amplitudes as λ_z increases. (This is the correct assumption for our MCC model, for example (see VF2004)). Then the maximum vertical wavelengths shown in Figure 6 represents the approximate GW vertical wavelengths that would be observed at a given altitude, since GWs with smaller vertical wavelengths would have been dissipated at lower altitudes, and GWs with larger vertical wavelengths would have relatively smaller amplitudes at that altitude and would therefore not be as readily observed. Thus we can assume for the purposes of this argument that $z_{\rm diss}$ represents the observed altitude and that the vertical wavelengths at $z_{\rm diss}$ represent the approximate observed vertical wavelengths. Then in the 115–160 km altitude range and for horizontal wavelengths of 100–500 km, we would predict observed vertical half wavelengths of ~4–23 km. These values fit well with the observed data, given the uncertainty in the observed temperature profiles and actual winds, as compared to our intrinsic results using canonical wind profiles.

[32] In Figure 7, we show the ratio $\lambda_z/\lambda_z(z_i)$ for the same GWs and model thermospheres as in Figure 6 in order to show which GWs have the largest increases in λ_z. The GWs with $\lambda_z(z_i) > 25$ km have the largest increases, while those GWs with $\lambda_z(z_i) < 20$ km have small or negligible increases. The increases are seen to be approximately proportional to the initial intrinsic frequency $\omega_{Ir}(z_i)$, with the largest increases occurring for GWs with $\omega_{Ir} \simeq N$. Typical increases

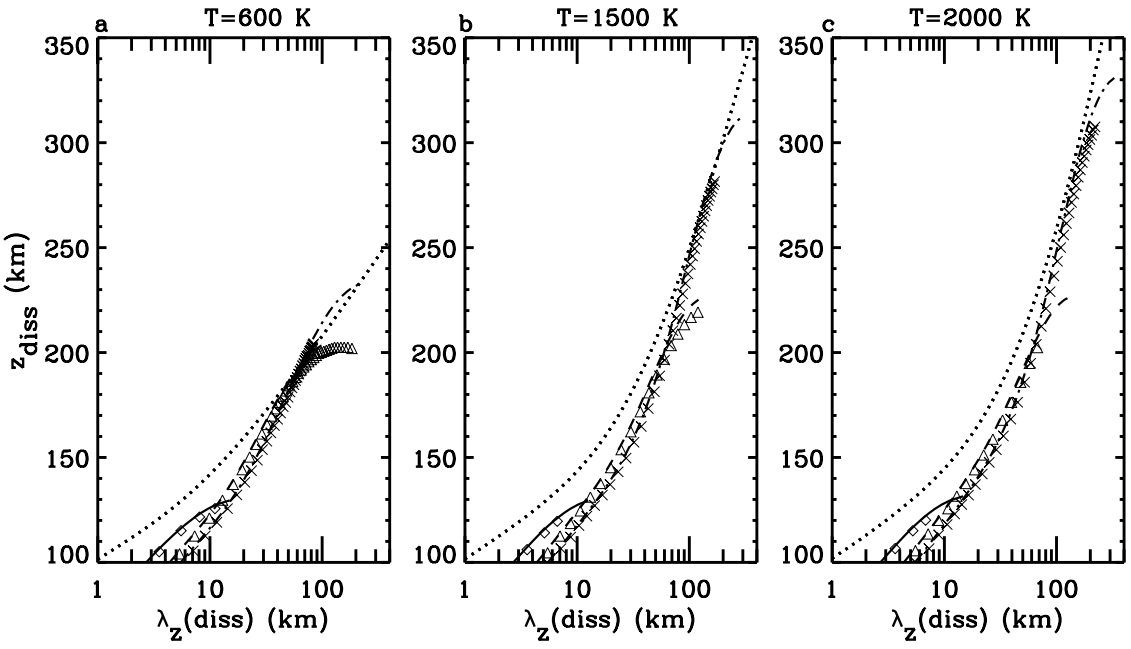

Figure 8. GW dissipation altitudes (y-axis) as a function of the GW vertical wavelengths at the dissipation altitudes (x-axis). GWs with λ_x = 10 km, λ_x = 75 km, and λ_x = 205 km are shown by diamonds, triangles, and crosses, respectively. (a) $\overline{T}_{max}$ = 600 K (profile II); (b) $\overline{T}_{max}$ = 1500 K (profile IV); (c) $\overline{T}_{max}$ = 2000 K (profile V). The solid, dash, and dash-dot lines show the quenching criteria for λ_x = 10 km, λ_x = 75 km and λ_x = 205, respectively, using equation (24) iteratively until the change in m_a is less than 1%. The dot lines show the minimum vertical wavelengths given by equation (27) from *Hines* [1964].

are a factor of 2–3 for GWs with $\omega_{Ir} > 0.2N_0$ and $\lambda_z(z_i) >$ 25 km, where the maximum increases shown in Figures 7a, 7b, and 7c are 3.4, 3.9, and 4.2, respectively. Note that in the absence of dissipation, the ratio $\lambda_z/\lambda_z(z_i)$ would be the same in each plot regardless of GW intrinsic parameters.

[33] In Figure 8, we show λ_z(diss) as a function of z_{diss} for the GWs shown in Figure 6 with λ_x = 10, 75, and 205 km as diamonds, triangles, and crosses, respectively. Here, λ_z(diss) is the vertical wavelength of the GW at z_{diss}. Again, λ_z(diss) increases as z_{diss} increases for constant λ_x, and as $\overline{T}$ increases, the penetration altitudes increase substantially. During active solar conditions, the penetration altitudes reach 310 km for these particular GWs. We also overlay the theoretical results for λ_z using equation (24) iteratively (with equation (25) being the initial guess for m_a until convergence is obtained for m_a within 1%). The theoretical results accurately predict λ_z, even in the lower thermosphere where $\overline{T}$ increases rapidly, and even for large $\lambda_z(z_i)$. Note that the GWs with λ_x = 10 km dissipate at $z \sim 100$ km with $\lambda_z \simeq 3$ km, and dissipate at $z \sim 115$ km with $\lambda_z \simeq 5$ km. These results agree well with the smallest λ_z observed at these altitudes [*Hines*, 1964; *Djuth et al.*, 1997]. We also overlay an expression relating the minimum GW vertical wavelengths to the viscosity [*Hines*, 1964]:

$$\lambda_z \simeq 2(3)^{3/4}\pi^{3/2}\nu^{1/2}N^{-1/2}. \quad (27)$$

This expression was derived under the assumption that $\lambda_z <$ H and that the background temperature is isothermal, using a perturbation expansion analysis for small ν. These curves underpredict the GW vertical wavelengths, as expected because of the underlying assumption involved in its derivation.

4. Thermospheric Effects From a Single Convective Plume

[34] In the previous section, we examined how temperature, shear effects, and dissipation alter the structure and dissipation altitudes for individual GWs. However, the behavior of individual GWs does not yield information about the role lower atmospheric sources of GWs have in altering the thermosphere. In this and in the next section therefore we employ spectra of GWs generated from our tropospheric MCC model in order to investigate the role deep convection may play in thermospheric dynamics.

[35] As GWs from deep convection propagate into the thermosphere, they are eventually removed from the spectrum via critical level filtering, evanescence, or dissipation. When GWs dissipate in the thermosphere, momentum flux divergence occurs, and body forces arise. Because the density decreases rapidly with altitude, those GWs dissipating at the highest altitudes achieve the largest increase in momentum flux (per unit mass) prior to dissipating. As Figure 6 suggests, those GWs having the largest vertical wavelengths, but having frequencies near the smaller buoyancy frequency in the thermosphere, are the GWs that can reach the highest altitudes. However, there may not be enough large λ_z GWs in the source spectrum (or in the GW spectrum after it passes through intervening winds) with these characteristics to yield significant accelerations in the thermosphere, though they may still be observed prop-

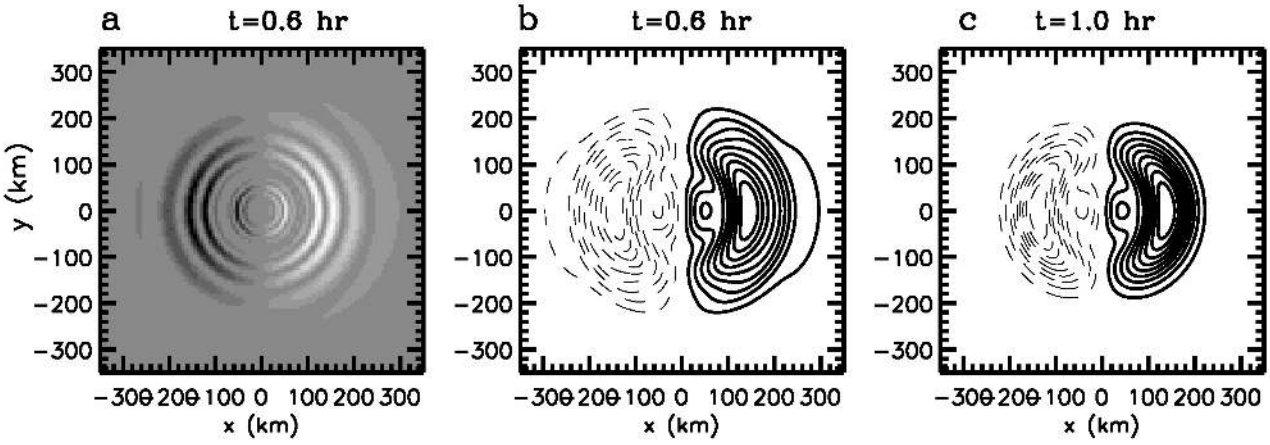

Figure 9. GW momentum fluxes at z = 90 km scaled by altitude, $\overline{u'w'}$ exp((z − 14 km)/H), for the deepest plume from the MCC model at (a) t = 0.6 hours; (b) t = 0.6 hours; (c) t = 1.0 hours. The contours in Figures 9b and 9c show positive (solid) and negative (dashed) values and are in intervals of 0.1 of the maximum values which are $\overline{u'w'}$ exp((z − 14 km)/H) = 9 and 22 m^2 s^{-2}, respectively.

agating to the highest altitudes. If a lower atmospheric GW spectrum is weighted toward small vertical wavelengths, the altitudes of the generated thermospheric body force may not necessarily be the highest achievable altitude but may instead depend sensitively on the thermospheric temperature profile, GW source spectrum, and intervening shears. This may result in a maximum body force that occurs many tens of kilometers below the highest achievable altitude for individual GWs in the spectrum.

[36] In VF2004, we found that a few of the deepest convective plumes within the modeled MCC contribute the most to the total momentum flux divergence in an isothermal atmosphere, that the deepest convective plume contributed more than any other plume, and that the contribution from the deepest plume achieved the highest altitude. Therefore in this section we study the GW momentum fluxes and body forces that result during extreme solar minimum and active solar conditions from this deepest plume only, in order to begin to understand what role the solar cycle plays in the thermospheric dynamics resulting from this idealized convection model. The deepest convective plume in the MCC model (plume 8 from VF2004) is created from a vertical body force with duration σ_t = 0.257 hours, $\mathcal{D}_x = \mathcal{D}_y$ = 17.8 km, and $\mathcal{D}_z$ = 11.6 km. This yields a convective plume with a maximum vertical updraft velocity of ~5.8 m s^{-1}. For diagnostic purposes in this section, we locate this vertical body force at $x = y = 0$ and z = 14 km and start the forcing at t = 0. Prior to studying the thermospheric effects, we normalize the spectral momentum fluxes from our ray trace model in an isothermal atmosphere via comparison with the real space, isothermal solutions to our convection model near the mesopause.

4.1. Normalization of the Fourier GW Momentum Flux Amplitudes

[37] Figures 9a, 9b, and 9c show the GW momentum fluxes (per unit mass) at z = 90 km arising from the deepest convective plume in the MCC, as calculated at t = 0.6 (gray scale) and at t = 0.6 and 1.0 hours using solid contours. This solution is calculated from the Boussinesq vertical body force model, as described in section 2.1. Implicit in this model is $\overline{T}$ = *constant*, H ≃ ∞, and $U = V = \mu = 0$. Here, the zonal and vertical velocities are multiplied without spatial averaging. Because we will compare these solutions with the ray trace results that utilize temporally averaged GW amplitudes, we must average these solutions temporally also. Noting that the zonal (u') and vertical (w') components of the GW velocity are in phase and are oscillatory at a single location (e.g., sin^2 in time), we average this solution (and the rest of the real space solutions in this section) temporally by dividing it by a factor of two. Rings of momentum flux are seen radiating away from the forcing region, with positive values for eastward propagating GWs and negative values for westward propagating GWs. The circular rings indicate that the vertical body force acts like a point source generator of GWs [*Lane and Reeder*, 2001; *Lane et al.*, 2001; *Piani et al.*, 2000; *Horinouchi et al.*, 2002; VF2004].

[38] We now compare the results from Figure 9 with the results from our ray trace model which integrates the ray paths and structure changes for GWs and calculates their changing spectral momentum fluxes $\widetilde{\overline{uw}}\ dk\ dl\ dm$. As motivated by Figure 9, we assume that the vertical body force acts like a point source generator of GWs and so launch all GWs from the center of the vertical body force at $t = \sigma_t/2$, where the force amplitude is maximum. Because the GWs from the vertical body force do not actually originate from the center of the plume at the same instant in time, we do not calculate the GW phases using this method. Each GW is ray traced through an isothermal atmosphere (temperature profile I) with zero dissipation. As it propagates through the stratosphere, mesosphere, and thermosphere, we bin its average momentum flux in x, y, z, and t with bin sizes Δx, Δy, Δz, and Δt, respectively.

[39] The binned GW momentum fluxes are shown in Figure 10 at the same altitude and approximate times as in Figure 9. Although the distinct ring patterns are not present due to the lack of phase information, the circular shape and location of the GW rings are similar to that from the Boussinesq model. Because the momentum fluxes from the ray trace model must be equal to the momentum fluxes from the Boussinesq model, we divided the binned, spectral

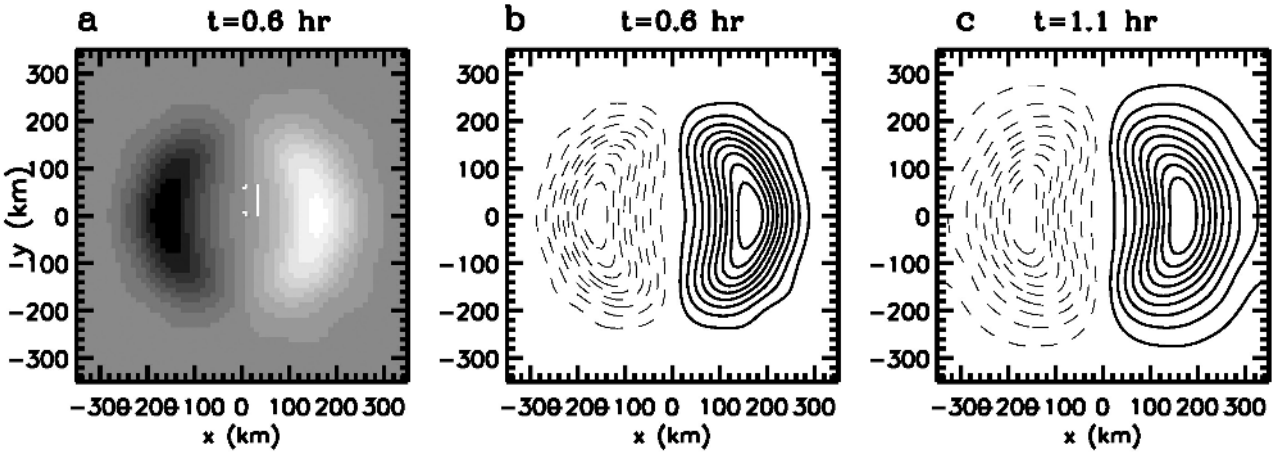

Figure 10. Binned and averaged GW momentum fluxes, $\overline{u'w'}$, at z = 90 km after ray tracing the GWs obtained from the Boussinesq spectral solution with no dissipation. The times shown are approximately the same as in Figure 8. The contours in Figures 10b and 10c show positive (solid) and negative (dashed) values and are in intervals of 0.1 of the maximum values which are $\overline{u'w'} \simeq 5$ and 30 m^2 s^{-2}, respectively. These fluxes are computed using equation (29).

momentum fluxes, $\overline{\widetilde{u}\widetilde{w}}\, dk\, dl\, dm$ (which have units of momentum flux times a volume factor), by the volume factor

$$\xi = \Delta x \Delta y \Delta z \Delta t / (80\ \text{s}). \tag{28}$$

This results in binned GW momentum fluxes (per unit mass) of

$$\overline{u'w'}(x,y,z,t) = \Sigma\left(\overline{\widetilde{u}\widetilde{w}}\, dk\, dl\, dm\right)/\xi, \tag{29}$$

where the sum is over all GWs that enter this bin during the given time and location intervals. The normalization volume factor ξ is used for the rest of the figures in this paper.

[40] In Figure 11, we show the maximum GW momentum fluxes at z = 90 km as a function of time for the ray trace model as small asterisks linked by a solid line. Results from the Boussinesq model at the same altitude but with varying x, y, and z grid sizes (again multiplied by 1/2 to account for temporal averaging) are shown as triangles, diamonds, squares, and crosses. This figure shows that the ray trace model (normalized as given by equation (29)) and various Boussinesq models all yield the same results for times less than 1 hour. For times greater than 1 hour, however, the Boussinesq models yield different results from each other and from the ray trace model and consistently overestimate the GW momentum fluxes. This is because the Boussinesq model has periodic boundary conditions, and GWs (and their momentum fluxes) are not able to "escape" the initial source domain. The ray trace model, on the other hand, does not have periodic boundary conditions; once a GW leaves the domain, it is eliminated from the GW spectrum. Therefore the ray trace model better represents the momentum fluxes at z = 90 km for times greater than 1 hour.

4.2. Effects of the Deepest Convective Plume on the Thermosphere

[41] Now that we determined the volume factor needed to normalize the spectral momentum flux magnitudes, we can explore the effects that the deepest convective plume in our MCC model has on the thermosphere during extreme solar minimum and active solar conditions using the ray trace model. A canonical lower atmosphere shear of $\overline{U}$ = 20 m s^{-1} (using equation (20)) is implemented for this purpose. Since a GW spectrum from the Boussinesq model is calculated in the intrinsic frame of reference, we subtract the background wind value at the initial location of the generated GWs. Figure 12a shows altitude profiles of momentum flux for the GW spectrum arising from this

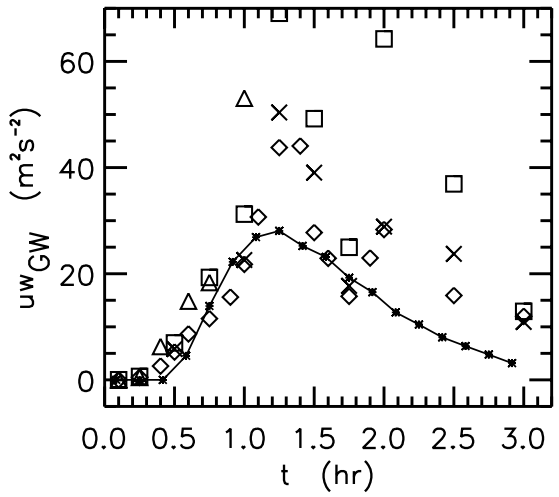

Figure 11. GW zonal momentum fluxes as a function of time at $z \simeq$ 90 km for the isothermal temperature profile I with zero dissipation. The small asterisks linked by a solid line denote the binned and averaged fluxes obtained from the ray trace solution as given by equation (29). The triangles, diamonds, squares, and crosses denote four differing Boussinesq solutions, scaled by exp((z − 14 km)/H), having various horizontal and vertical grid sizes with 128 × 128 × 256 grid points in the x, y and z directions, respectively. The diamonds denote the model used to create Figure 9 here and Figure 6 in VF2004.

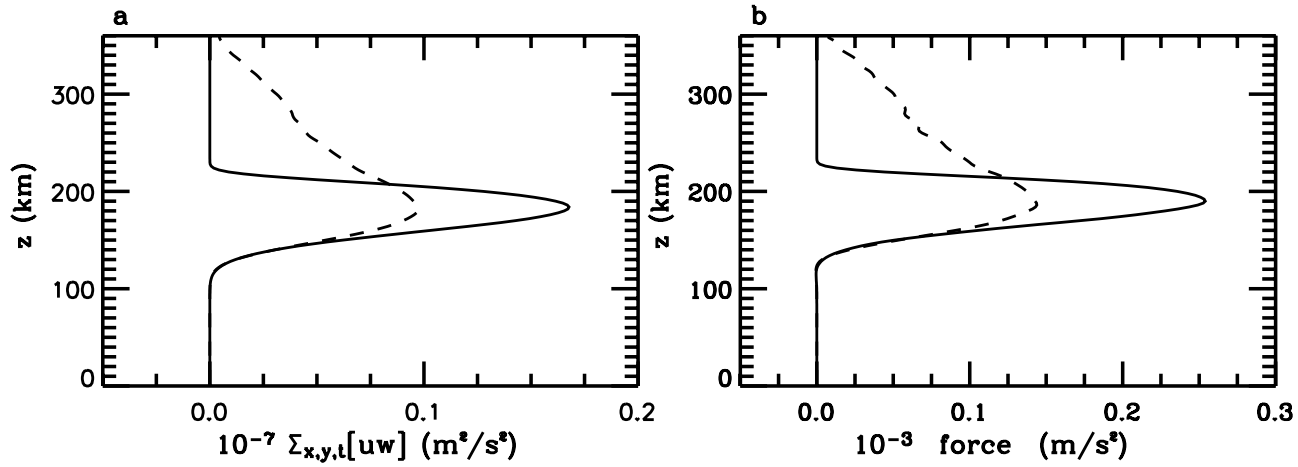

Figure 12. Vertical profiles of the momentum fluxes (a) and body forces (b) arising from the dissipation of GWs from the deepest convective plume. The temperature profiles are II (solid lines) and V (dash lines). The momentum flux and body force profiles are multiplied by 10^{-7} and 10^{-3}, respectively. All profiles are summed horizontally and temporally.

plume. The body forcing accompanying wave dissipation is displayed in Figure 12b, and is calculated via

$$F_b = -\frac{1}{\overline{\rho}} \frac{\partial(\overline{\rho} u' w')}{\partial z}. \quad (30)$$

In this case, horizontal and temporal sums are performed on the momentum fluxes prior to calculating this vertical derivative. The momentum flux profile is positive because the shear imposes significant anisotropy on the surviving GWs (as described in Figure 3) so that westward propagating GWs are red-shifted to lower frequencies and vertical wavelengths, while eastward propagating GWs are blue-shifted to higher frequencies and larger vertical wavelengths. The average body force peaks at $z \simeq 190$ km during both extreme solar minimum and active solar conditions. However, there is significant body forcing up to $z \sim 360$ km during active solar conditions, whereas the body forcing is confined below $z \simeq 230$ km during extreme solar minimum.

[42] Figure 13a shows a horizontal cross-section of the GW momentum flux in the thermosphere from this convective plume during extreme solar minimum at its peak of $z \simeq 184$ km and $t \simeq 1.4$ hours. The momentum flux is mostly positive, with a small negative component. The percentage of negative as compared to positive momentum flux depends on the shear. The larger the shear, the smaller the negative flux as compared to positive flux at the peak

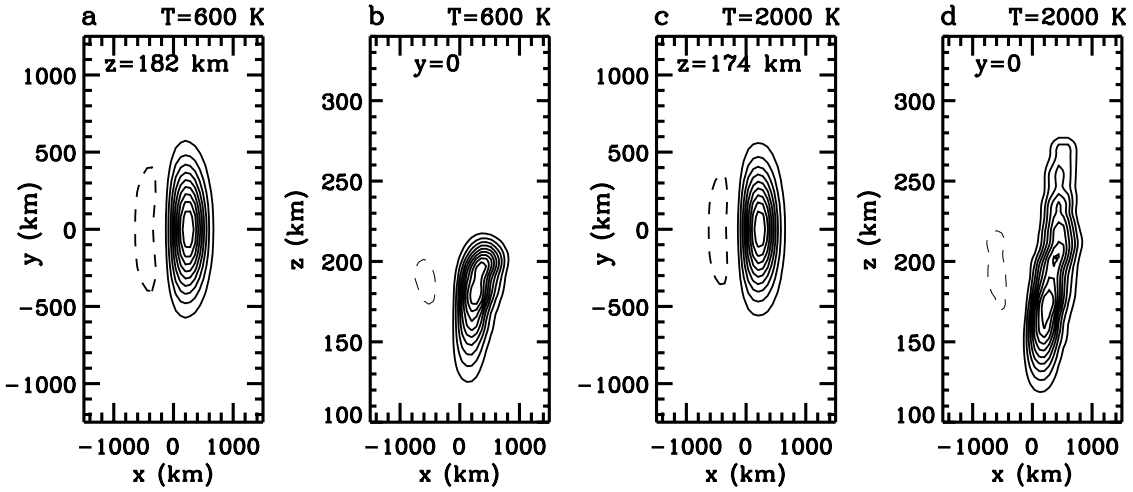

Figure 13. GW momentum flux profiles for the deepest convective plume (a–b) during extreme solar minimum (profile II) and (c–d) during active solar conditions with profile V. Figure 13a shows horizontal cross-section at $z \simeq 182$ km and $t \simeq 1.4$ hours, with a maximum of 7000 $m^2\ s^{-2}$; Figure 13b shows vertical cross-section at $y = 0$ and $t \simeq 1.4$ hours, with a maximum of 9000 $m^2\ s^{-2}$ at $z \simeq 180$ km; Figure 13c shows horizontal cross-section at $z \simeq 174$ km and $t \simeq 1.4$ hours, with a maximum of 3600 $m^2\ s^{-2}$; Figure 13d shows vertical cross-section at $y = 0$ and $t \simeq 1.4$ hours, with a maximum of 4000 $m^2\ s^{-2}$ at $z \simeq 173$ km. Each cross-section is plotted in intervals of 0.1 times the maximum value.

altitude. Although the convective plume is 9 km ×9 km full width half max in the troposphere, the momentum flux distribution is spread out horizontally to 600 km × 600 km full width half max in the thermoshere because of wave dispersion of GW components with differing frequencies (similar to *Hines* [1967]). Figure 13b shows a vertical cross section of the GW momentum flux during extreme solar minimum. The momentum flux is only significant for $z <$ 230 km. The peak of this distribution occurs at $x \simeq 200-300$ km and $z \simeq 170-200$ km. Since the GWs originate from $x = 0$ and $z = 14$ km, those with frequencies close to the smaller buoyancy frequency in the thermosphere (e.g., $\overline{N} = 0.6N_0$ for this temperature profile) are likely the dominant contributors to the total momentum fluxes. This is because a GW with angle θ to the vertical satisfies $\omega_{Ir}/N_0 \simeq \cos\theta$, or

$$\omega_{Ir}/N_0 \sim \cos\left(\tan^{-1}\left(x/(z-14\text{ km})\right)\right) \tag{31}$$

if zonally propagating. Using Figure 6a, high-frequency GWs dissipate at $z_{diss} \geq 170$ km when $\lambda_z(z_i) > 25$ km. Importantly, high-frequency GWs with $\lambda_x \sim 50-80$ km and $\lambda_z(z_i) \sim 45-55$ km dissipate at $z \simeq 184$ km, which is the altitude of the maximum GW momentum fluxes from the convective plume. Prior to dissipating, these GWs have increased maximum vertical wavelengths of $\lambda_z \sim 75-125$ km (or higher). Additionally, the estimated time taken for these GWs to reach $z \simeq 184$ km is $[(184-14)10^3/(30-40)]$ s $\sim$ 1.2–1.6 hours, which is the approximate time that the GW momentum fluxes achieve a maximum. Here we estimated the vertical group velocity for these GWs to be (30–40) m s^{-1} (see Figure 7 from VF2004).

[43] During active solar conditions with $\overline{T} = 2000$ K, the GW momentum flux distribution peaks at somewhat lower altitudes at the same time and with 1/2 the amplitude, as shown in Figure 13c–13d. The somewhat lower altitude is likely due to the structure of the temperature profile V in the lower thermosphere as compared to profile II. The maximum occurs for $x \simeq 200-300$ km. This implies that these GWs also have intrinsic frequencies close to the thermospheric buoyancy frequency, $\overline{N} \simeq 0.35N_0$, since the GWs here have very steep propagation paths above $z \sim 120$ km. Using Figure 6c, high-frequency GWs with $\lambda_x \sim 60-90$ km and $\lambda_z(z_i) \sim 25-30$ km dissipate at $z \simeq 174$ km, which is the altitude of the maximum GW momentum fluxes from the convective plume in this temperature structure. Prior to dissipating, these GWs have increased maximum vertical wavelengths of $\lambda_z \simeq 45-55$ km. Although the initial amplitudes are larger for these GWs than for the GWs with $\lambda_x \sim 50-80$ km and $\lambda_z(z_i) \sim 45-55$ km (see Figure 7 of VF2004), the peak momentum fluxes are larger during extreme solar minimum than during active solar conditions because the density is smaller and ν is larger at $z \sim 180$ km, thereby creating a strongly dissipative environment through which few GWs can pass. During active solar conditions, however, ν is small enough at $z\sim180$ km to allow many GWs to propagate to higher altitudes, thereby decreasing the amplitude of the total maximum GW momentum flux at $z \sim 180$ km. Note that the horizontal cross section at $z \simeq 300$ km and $t \simeq 1.6$ hours during active solar conditions shows a distribution which is 50% wider meridionallly, but is virtually unchanged zonally (not shown).

[44] As discussed above, GW dissipation results in momentum flux divergence and thermospheric body forcing. Figure 14 shows a time series of the resulting body forces during extreme solar minimum (upper row) and active solar conditions (lower row). The body forces are calculated using equation (30). Figures 14a–14d shows the body forces at the altitude and times containing the maximum body force amplitude. The body force lasts for 0.5–1 hours and has a horizontal size of ∼600 km × 600 km at full width half max. During active solar conditions, the body force distribution at the same altitude looks similar to Figures 14a–14d (except having an amplitude that is ∼50% smaller) and is therefore not shown here. Instead, Figures 14e–14h shows the body forces during active solar conditions at the higher altitude of $z \simeq 240$ km. Although the body force amplitude is smaller, and the temporal duration is somewhat longer than during extreme solar minimum, the horizontal cross sections look similar to Figures 14a–14d.

[45] During extreme solar minimum, the maximum body force amplitude is ≃1 m s^{-2} at $z = 200$ km. However, this amplitude would be reduced by a factor of 2 or 3 if the spectrum propagated through realistic mesospheric and lower thermospheric winds [*Hines and Reddy*, 1967]. Therefore we estimate a maximum body force amplitude of ≃0.15–0.25 m s^{-2} at full-width half max, which implies full-width half max accelerations of ≃500–750 m s^{-1} hr^{-1}. During active solar conditions, the amplitude is a factor of 2 smaller at the same altitude. These accelerations are very large but only last for 0.5–1 hours. It is possible these large, intermittent body forces, and their associated vertical motions, could contribute to the seeding of ESF and spread-F bubbles, although studies have yet to be performed to investigate this mechanism.

[46] Figure 15 shows time series of vertical profiles of the body forces during extreme solar minimum (Figure 15a) and during active solar conditions (Figure 15b). These profiles are calculated at $x \simeq 280$ km and $y = 0$ km, which are the horizontal coordinates of the maximum body force. During extreme solar minimum, the profiles peak at $z \simeq$ 190 km at early times, at 200 km a little later, and at 180 km later still. During active solar conditions, the profiles peak at $z \simeq 160$ km at early times, at 200 km a little later, then at 180 km later still. The increasing height of the body force at early times may be due to transience caused by a propagating GW packet which has not yet dissipated. At $t \sim 1.4$ hours, the body forces during both extreme solar minimum and active solar conditions reach maximum altitudes of $z \sim 200$ km. Thereafter, their altitudes decrease with time. This is because GW dissipation at later times at this location is caused by slower GWs having smaller λ_z, smaller vertical group velocities, and lower dissipation altitudes.

[47] The high-altitude tail of the body force distribution during active solar conditions extends at least to $z \sim 360$ km (see Figure 12b). This tail is likely composed of GWs having intrinsic frequencies nearly equal to the buoyancy frequency in the thermosphere of $\omega_{Ir} \sim 0.35N_0$ and with initially large vertical wavelengths. Because the anelastic condition is $\lambda_z < 715$ km when $\overline{T} = 2000$ K, GW vertical wavelengths can become quite large without violating this condition. Owing to their much larger vertical wavelengths and to the slower increase in kinematic viscosity with

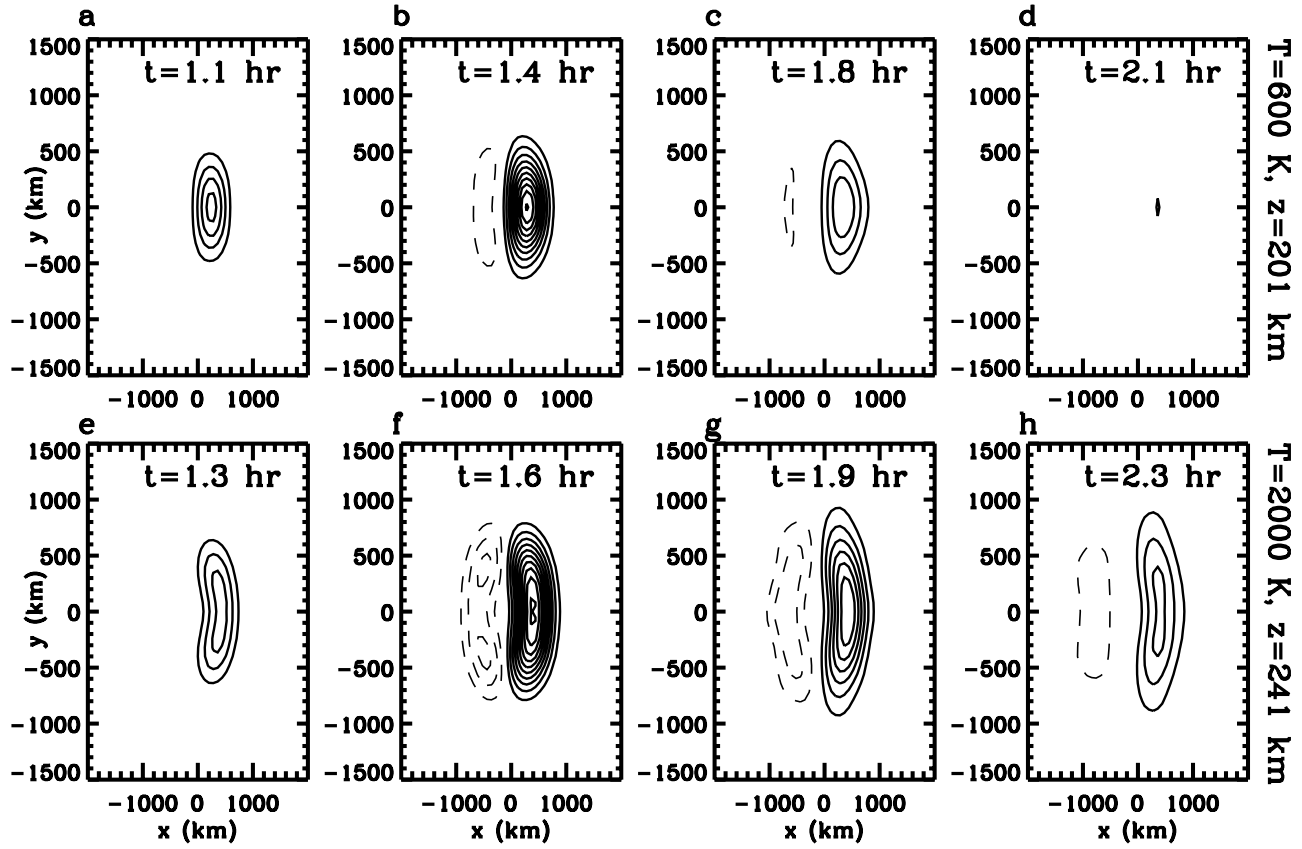

Figure 14. Time series of the body force in the thermosphere from the deepest convective plume which arises from GW momentum flux divergence via dissipation. We show these body forces during extreme solar minimum (profile II) at $z \simeq 200$ km in the upper row, and for active solar conditions with profile V at $z \simeq 240$ km in the lower row. The times for each plot are labeled. Each cross section shows positive (solid) and negative (dashed) values and is plotted in intervals of 0.1 times the maximum value for the row. The maximum force in Figures 14a–14d is $\simeq 1.1$ m s^{-2}, and the maximum force in Figures 14e–14h is 0.25 m s^{-2}. Note that the body force is maximum ~50 km lower in altitude for profile V.

altitude, these GWs can propagate much higher before dissipating. Although they may not contribute substantially to the momentum flux divergence and body forcing in the thermosphere, they could be observed propagating to very high altitudes within the thermosphere.

5. Effects of All Convective Plumes in the MCC on the Thermosphere

[48] Now that we have a good understanding of how the deepest plume in the MCC affects the thermosphere, we investigate how the thermosphere responds to all of the convective plumes in the MCC model. We assume that each convective plume (i.e., vertical body force) generates its own GW spectrum and that the spectra from neighboring vertical body forces are incoherent. This was shown to be a good approximation for simultaneous body forces that are separated by more than their diameter (VF2004). For each vertical body force centered at location (x_0, y_0, z_0) and time t_0, we calculate the spectral momentum fluxes for the GWs and ray trace the GWs from location (x_0, y_0, z_0) and time t_0. Figure 16 shows altitude profiles of momentum flux (Figure 16a) and body forcings (Figure 16b) accompanying wave dissipation which arise from this MCC. The profiles are summed horizontally and temporally as in Figure 12. Both momentum flux and body force profiles are larger than for the deepest plume by a factor of ~4 due to the presence of several other large plumes and many small plumes within the MCC (see Figure 12). Otherwise, the profiles look very similar.

[49] Figure 17a shows a horizontal cross section of the GW momentum flux from this MCC during extreme solar minimum at its peak of $z \simeq 180$ km and $t \simeq 1.9$ hours. As with the single deep convective plume, the momentum flux is mostly positive, with a small negative component. However, here the momentum flux is a factor of 3 larger in magnitude due to the larger GW variances that are excited from the entire complex as opposed to just the deepest convective plume. Note that the maximum occurs ~30 minutes later than for the single convective plume because the GWs were excited at $t \sim 0$–15 min there whereas here the average excitation time is $t \sim 30$–45 min. A vertical slice during extreme solar minimum is shown in Figure 17b. Comparison of Figures 17a–17b with Figures 13a–13b shows that the horizontal and vertical profiles look nearly identical (except for the amplitude change). Figures 17c–17d shows the horizontal cross section of the GW momentum flux at its peak during active solar conditions at $z \simeq 170$ km and $t \simeq 1.9$ hours, and a

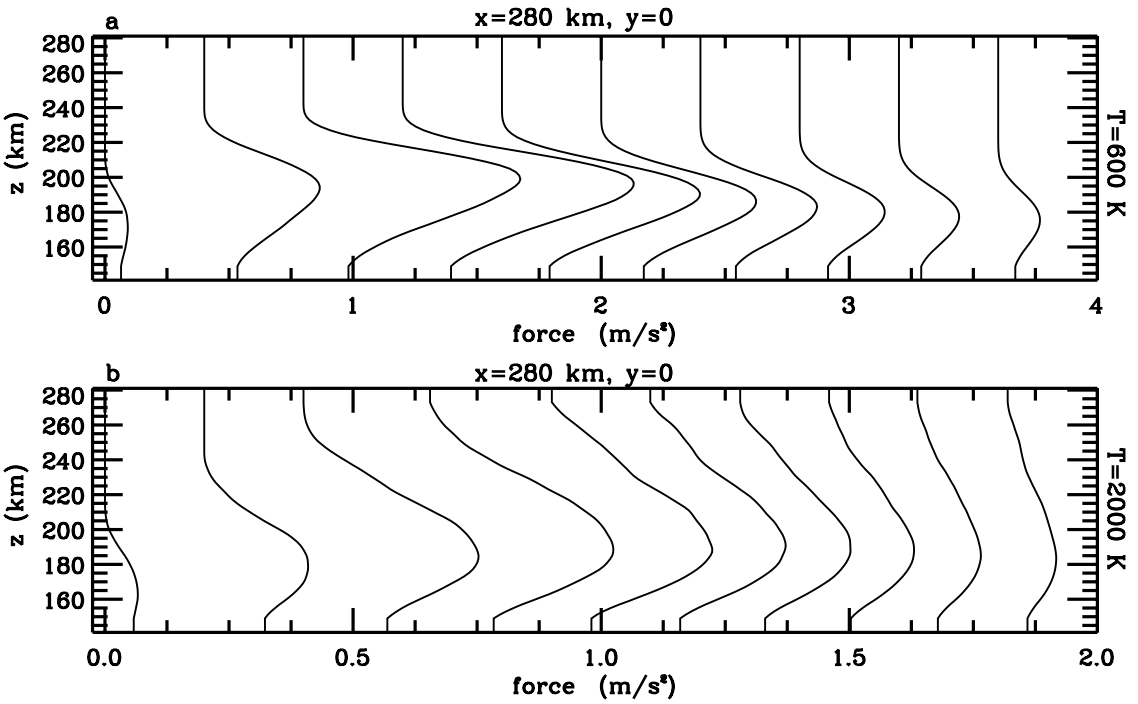

Figure 15. Accelerations created by GW dissipation in the thermosphere resulting from the deepest convective plume. (a) Extreme solar minimum (profile II) at $x \simeq 280$ km and $y = 0$. The times shown are equally spaced in increments of 0.2 hours between the starting time $t \simeq 0.9$ hours and the ending time $t \simeq 2.4$ hours. Each plot is offset by 0.4 m s^{-2}. This body force is maximum at $x \simeq 280$ km, $y = 0$, $z \simeq 200$ km, and $t \simeq 1.4$ hours. (b) Active solar conditions with temperature profile V at $x \simeq 280$ km and $y = 0$. The times shown are equally spaced in increments of 0.2 hours between the starting time $t \simeq 0.9$ hours and the ending time $t \simeq 2.4$ hours. Each plot is offset by 0.2 m s^{-2}. This body force is maximum at $x \simeq 280$ km, $y = 0$, $z \simeq 190$ km, and $t \simeq 1.6$ hours. Note that the x-axis scales are different for Figures 15a and 15b.

vertical slice of the GW momentum flux, respectively. Comparing with Figures 13c–13d, except for being larger in magnitude by a factor of 3, the GW momentum flux profiles look very similar to those from the deepest convective plume. Therefore the GWs that contribute most to the maximum GW momentum fluxes for the MCC are nearly the same as those from the deepest convective plume during extreme solar minimum and active solar conditions; their horizontal and vertical scales were discussed in section 4.2.

[50] Figure 18 shows time series of the resulting thermospheric body forces during extreme solar minimum (upper row) and active solar conditions (lower row). Comparing Figures 18a–18d with Figures 13a–13d, we note that the body force from the MCC is twice as strong and 10–15 km lower in altitude than the body force from the deepest convective plume. The lower altitude occurs because most of the convective plumes in the MCC are shallow and therefore excite GWs with primarily small vertical wave-

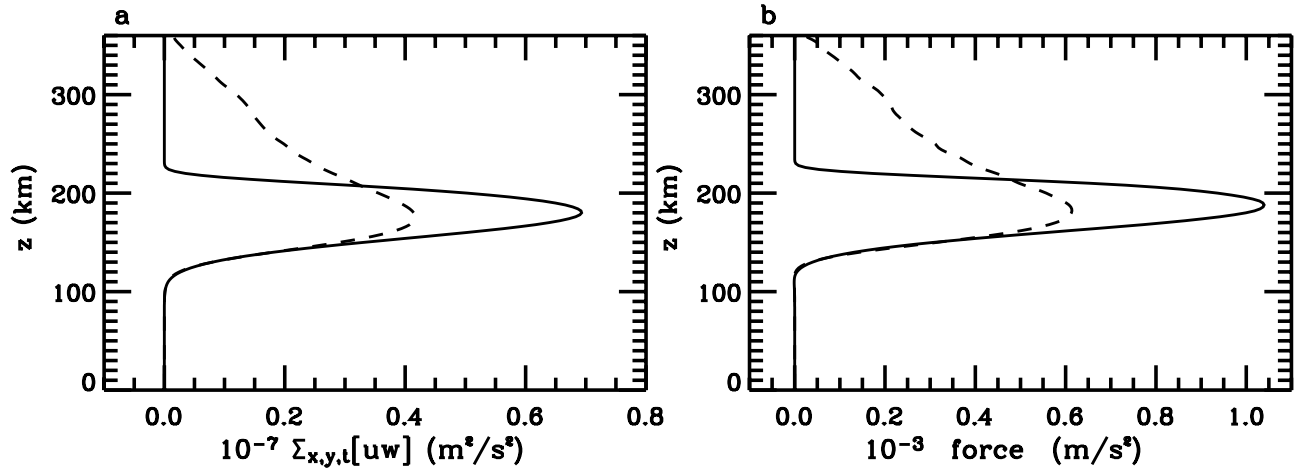

Figure 16. Same as for Figure 12, but for all of the convective plumes in the MCC.

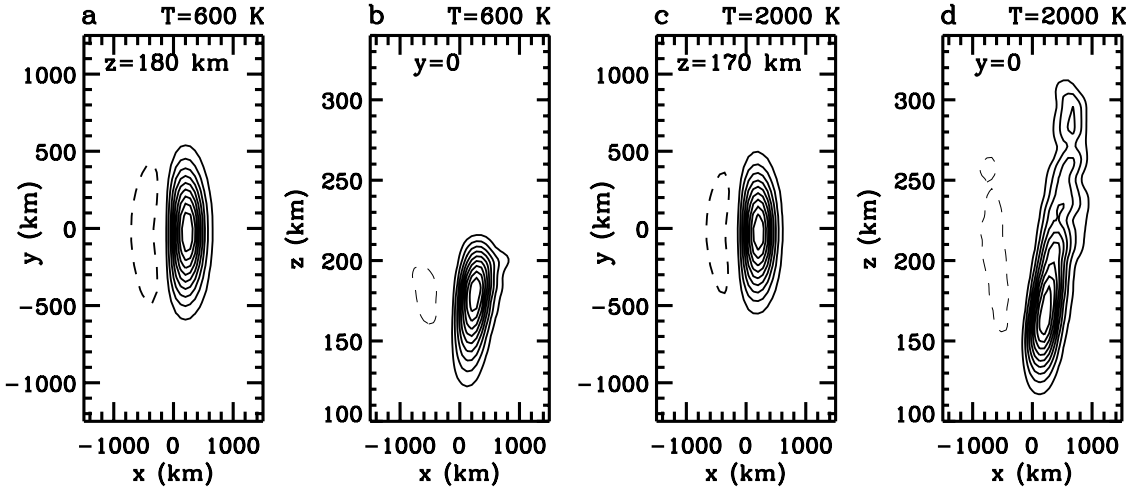

Figure 17. GW momentum flux profiles for all of the plumes in the MCC during (a–b) extreme solar minimum (profile II) and (c–d) during active solar conditions with profile V. Figure 17a shows horizontal cross-section at $z \simeq 180$ km and $t \simeq 1.9$ hours, with a maximum of 22000 $m^2\ s^{-2}$; Figure 17b shows vertical cross-section at $y = 0$ and $t \simeq 1.9$ hours, with a maximum of 27000 $m^2\ s^{-2}$ at $z \simeq 180$ km; Figure 17c shows horizontal cross-section at $z \simeq 170$ km and $t \simeq 1.9$ hours, with a maximum of 13000 $m^2\ s^{-2}$; Figure 17d vertical cross-section at $y = 0$ and $t \simeq 1.9$ hours, with a maximum of 15000 $m^2\ s^{-2}$ at $z \simeq 165$ km. Each cross-section is plotted in intervals of 0.1 times the maximum value, as in Figure 13.

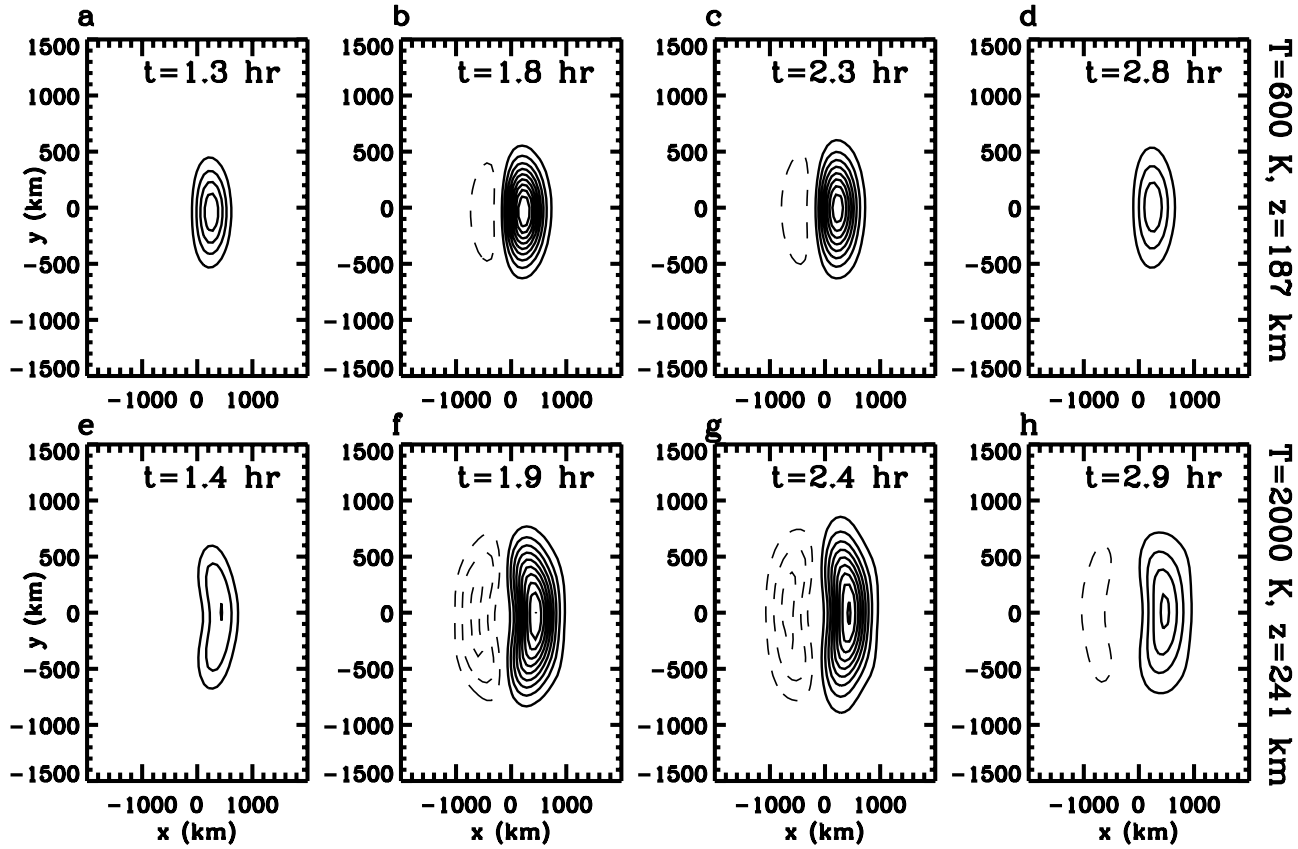

Figure 18. Time series of the thermospheric body forces resulting from the MCC which arises from GW momentum flux divergence via dissipation. We show these body forces during extreme solar minimum (profile II) at $z \simeq 190$ km in the upper row, and during active solar conditions with profile V at $z \simeq 240$ km in the lower row. The times for each plot are labeled. Each cross-section is plotted in intervals of 0.1 times the maximum value for the row, as in Figure 14. The maximum force in Figures 18a–18d is 3.0 m s^{-2}, and the maximum force in Figures 18e–18h is 1.0 m s^{-2}. Note that the body force is maximum ~60 km lower in altitude for profile V, where it has twice the amplitude.

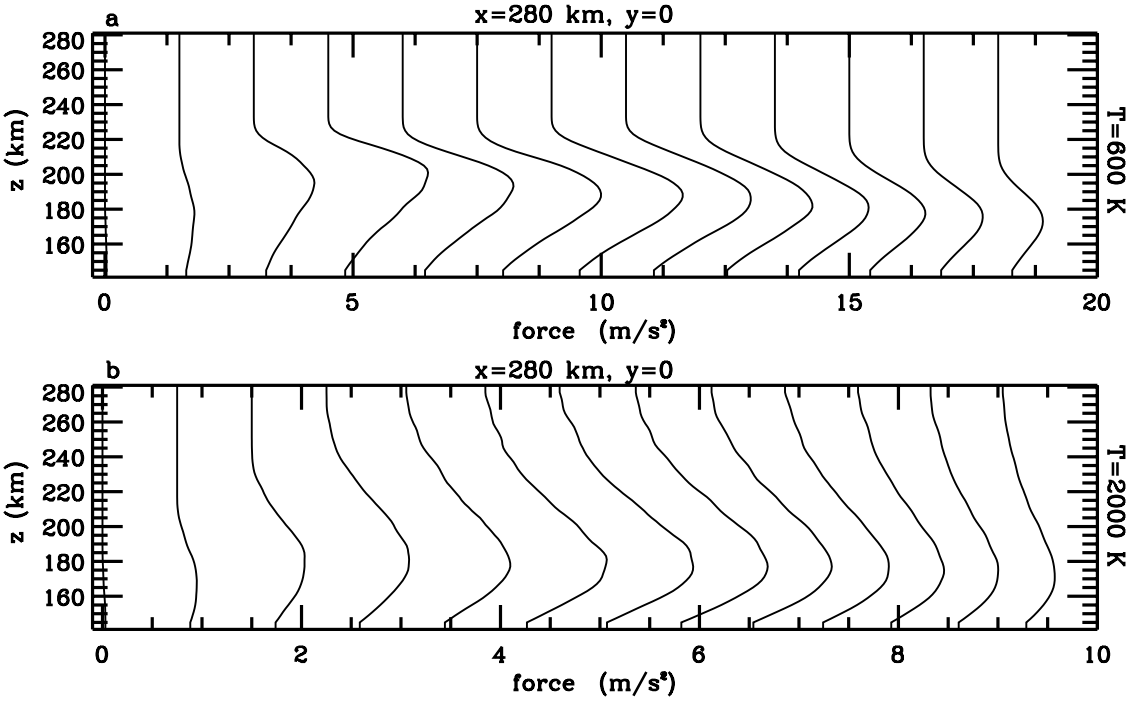

Figure 19. Accelerations created by GW dissipation in the thermosphere resulting from the MCC. The times shown are equally spaced in increments of ≃0.2 hours between the starting time $t \simeq 0.9$ hours and the ending time $t \simeq 2.9$ hours. (a) Extreme solar minimum (profile II) at $x \simeq 280$ km and $y = 0$. Each plot is offset by 1.5 m s^{-2}. This body force is maximum at $x \simeq 280$ km, $y = 0$, $z \simeq 187$ km, and $t \simeq 1.8$ hours. (b) Active solar conditions with profile V at $x \simeq 280$ km and $y = 0$. Each plot is offset by 0.75 m s^{-2}. This body force is maximum at $x \simeq 280$ km, $y = 0$, $z \simeq 185$ km, and $t \simeq 1.8$ hours. Note that the x-axis scales are different for Figures 19a and 19b.

lengths which dissipate lower in altitude. In addition, the body force resulting from the MCC lasts 1–1.5 hours because the duration of strong convection is 1 hour. Note that the thermospheric body force has a horizontal size of ∼600 km × 600 km at full width half max, similar to that from the deepest convective plume.

[51] During active solar conditions, the body forces at $z \simeq$ 187 km look similar to Figures 18a–18d (except having an amplitude that is ∼50% smaller), and is therefore not shown here. Instead, Figures 18e–18h shows the body force at $z \simeq 240$ km during active solar conditions. The body force is similar to Figures 13e–13h, except that the amplitude is larger by a factor of ∼3 when all the plumes contribute to the forcing.

[52] During extreme solar minimum, the maximum body force amplitude from GW dissipation in the thermosphere resulting from this MCC is ≃3 m s^{-2} at $z \simeq 200$ km. However, this amplitude might have been reduced by a factor of 2 or 3 if the spectrum had propagated through realistic mesospheric and lower thermospheric winds [*Hines and Reddy*, 1967]. Therefore we estimate a maximum body force of ≃0.5–0.75 m s^{-2} at full-width half max. This implies very large full-width half max accelerations of ≃2000–3000 m s^{-1} hr^{-1}. During active solar conditions, the amplitude is a factor of 2 smaller at a similar altitude. These accelerations are very large but only last for the duration of strong, deep convection (i.e., 1.0–1.5 hours for this model).

[53] Figure 19 shows time series of vertical profiles of the body force during extreme solar minimum (Figure 19a) and during active solar conditions (Figure 19b). These profiles are calculated at $x \simeq 280$ km and $y = 0$ km, which is the horizontal coordinate for the maximum body force. This figure shows that the body force is insignificant for $z > 230$ km during extreme solar minimum, as was the case for the deepest convective plume. During active solar conditions, however, there is more variability in the body force profiles at much higher altitudes.

[54] We now estimate the horizontal and vertical velocities of zonally propagating GWs in the thermosphere associated with this MCC. Using the Boussinesq solution $u' \sim -mw'/k = \pm\lambda_x w'/\lambda_z$ [*Kundu*, 1990], the GW momentum fluxes are $|\overline{u'w'}| \simeq (\lambda_x/\lambda_z)\ \overline{w'^2}$ so that the absolute value of the horizontal velocity is

$$|u'| \sim \sqrt{\frac{\lambda_x}{\lambda_z}|\overline{u'w'}|}. \tag{32}$$

The peak value during extreme solar minimum is $\overline{u'w'} \simeq$ 22000 m^2 s^{-2} (see Figure 17a). We reduce this amplitude by a factor of 2 or 3 to account for the spectrum propagating through realistic mesospheric and lower thermospheric winds [*Hines and Reddy*, 1967]. Therefore we conservatively use a full-width half max value of $\overline{u'w'} \simeq$ 3000–5000 m^2 s^{-2}. Since the peak in the momentum flux occurs at $x \sim$ 200–300 km, the GWs contributing to

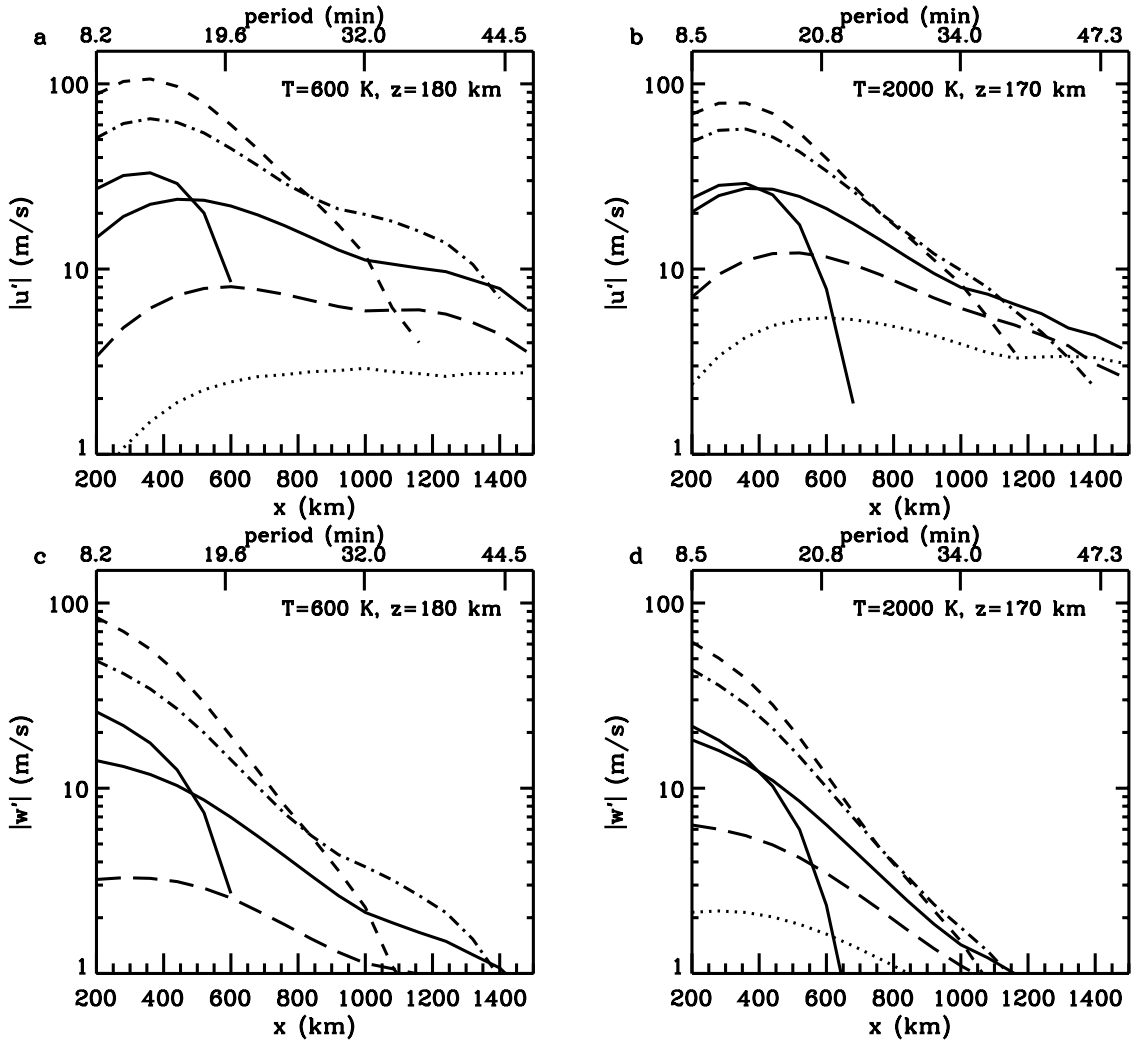

Figure 20. Estimated neutral (a and b)horizontal velocities $|u'|$ and (c and d) vertical velocities $|w'|$ for the GWs at $y = 0$ using equation (32). Figure 20a shows $|u'|$ at $z = 180$ km during extreme solar minimum (temperature profile II); Figure 20b shows $|u'|$ at $z = 170$ km during active solar conditions (temperature profile V); Figure 20c shows $|w'|$ at $z = 180$ km during extreme solar minimum (temperature profile II); Figure 20d shows $|w'|$ at $z = 170$ km during active solar conditions (temperature profile V). The solid, short dash, dash-dot, dash-dot-dot-dot, long dash, and dot lines refer to $t = 1.1$, 1.9, 2.8, 3.6, 4.4, and 5.3 hours after convective initiation. We use the values of $\overline{u'w'}$ shown in Figures 17a and 17c decreased by a factor of 3 to account for losses due to realistic, intervening winds in the mesosphere and thermosphere. The upper x-axis shows the estimated ground-based periods using the lower atmosphere value $N = 0.02$ s^{-1}. (Note that the ground based periods do not change as GWs propagate into the thermosphere through shears and temperature gradients).

this peak likely have $\lambda_x \sim (1-2)\lambda_z$ with ground-based periods of ~10 min. We then estimate full width half-max horizontal and vertical velocities of $u' \sim 40-140$ m s^{-1} and $w' \sim 40-70$ m s^{-1}, respectively, at the peak of the momentum flux distribution.

[55] Figure 20 shows the estimated neutral horizontal and vertical velocities for the GWs at the peak altitudes in Figures 17a and 17c during extreme solar minimum (Figures 20a and 20c) and active solar conditions (Figures 20b and 20d) before, during, and after the peak amplitude is achieved. The estimated GW periods range from 8 to 50 min and are located on the upper x-axis. In order to calculate λ_x/λ_z for equation (32), we determine ω/N approximately in the lower atmosphere using equation (31) (i.e., ignoring the steeper ray paths above the shear), and solve for K_{H^2/m^2} using equation (7). The small correction term 1/4 H^2m^2 is calculated using lower atmospheric values $\lambda_z \sim 50$ km and H = 7 km. The horizontal and vertical velocities are very large at $x \sim 300$ km and $t \sim 1.9-2.8$ hours for very high frequency GWs with periods of ~10–20 min, as estimated above. These velocities decrease with increasing x and wave period, however. Near the edges of the momentum flux distributions and for late times of $t > 4.4$ hours, the horizontal velocities are smaller, $u' < 2-10$ m s^{-1}, and the vertical velocities are very small, $w' \ll 1$ m s^{-1}. By $t \sim 5.3$ hours, there are only small horizontal and

vertical winds of $u' \sim 0-5$ m s^{-1} and $w' \sim 0-2$ m s^{-1} for all $x > 0$. For GWs with periods of 30–50 min, horizontal and vertical velocities range from $u' \sim 2-20$ m s^{-1} and $w' \sim 0-4$ m s^{-1}, depending on the time and wave period (or distance from the peak of the momentum flux distribution), with typical velocities ranging from $u' \sim 3-10$ m s^{-1} and $w' \sim 0-2$ m s^{-1}.

6. Conclusions and Discussion

[56] We found that GWs penetrate to much higher altitudes during active solar (and daytime) conditions than during extreme solar minimum (and nighttime) conditions using the more general GW anelastic dispersion relation of VF2005, as found earlier by previous researchers using other formulations [*Pitteway and Hines*, 1963; *Francis*, 1973; *Yeh et al.*, 1975; *Richmond*, 1978; *Cole and Hickey*, 1981]. This occurs not only because the kinematic viscosity increases less rapidly with altitude when the temperature increases but also because GW vertical wavelengths increase substantially. Using several temperature profiles and a ray trace model, we investigated propagation, dissipation altitudes, evanescence, and GW structure changes for individual GWs propagating from the lower atmosphere into the thermosphere. As the temperature in the thermosphere increases, the asymptotic buoyancy frequency decreases, and λ_z increases.

[57] When dissipation is ignored, because the asymptotic buoyancy frequency in the thermosphere N decreases by $\sqrt{\overline{T}_0/\overline{T}}$, therefore λ_z increases by $\sqrt{\overline{T}/\overline{T}_0}$ or greater, as determined by the dispersion relation. If the temperature in the lower atmosphere is $\overline{T}_0 = 250$ K, and the temperature in the thermosphere is $\overline{T} \simeq 600$ K and $\overline{T} = 2000$ K, then λ_z increases by $\sqrt{2}$ and $\sqrt{8}$, respectively, for those GWs with intrinsic frequencies that are much smaller than the buoyancy frequency in the thermosphere. Because the buoyancy frequency decreases in the thermosphere, any GWs with intrinsic frequencies that are greater than the buoyancy frequency at some altitude in the thermosphere become evanescent and reflect downwards. Thus GWs with very high frequencies in the lower atmosphere might not propagate into the middle thermosphere during active solar conditions, although they may reach these altitudes during extreme solar minimum. During extreme solar minimum, only GWs with intrinsic frequencies $\omega_{Ir} < 0.65N_0$ survive reflection, where N_0 is the buoyancy frequency in the lower atmosphere. During active solar conditions with $\overline{T} = 2000$ K, only GWs with intrinsic frequencies $\omega_{Ir} < 0.35N_0$ survive reflection. For GWs with intrinsic frequencies that are slightly smaller than the buoyancy frequency, we found that λ_z increases by more than $\sqrt{\overline{T}/\overline{T}_0}$. For example, if a lower atmospheric GW with $\lambda_z \simeq 60$ km propagates into an active solar thermosphere, then λ_z increases to $\simeq$150 km if $\lambda_x \geq 400$ km, but increases instead to $\simeq$300–325 km for $\lambda_x \simeq 170$ km.

[58] When we include the effects of dissipation, the vertical wavelengths of high frequency GWs still increase substantially in the thermosphere, especially for GWs with initially large vertical wavelengths of $\lambda_z > 25$ km, although the increase is not as large as when dissipation is neglected. This is because GWs typically dissipate at altitudes where the temperature is smaller than the asymptotic temperature. Additionally, the increase in λ_z is much larger during active solar conditions than during extreme solar minimum because of the larger asymptotic temperature, slower decrease of density with altitude, and increasing λ_z with altitude. GWs with $\omega_{Ir} \simeq N$ will have the largest increases in λ_z. Those GWs which barely escape evanescence and have $\lambda_x \sim 300-400$ km penetrate to altitudes of $z \simeq 350-450$ km before dissipating with very large $\lambda_z > 300$ km during active solar conditions (Vadas, submitted manuscript, 2006). Once a GW begins to dissipate, its vertical wavelength decreases rapidly.

[59] We then examined the response of the thermosphere to GWs from a single deep convective plume as well as from dozens of plumes in a mesoscale convective complex (MCC) model. We found that GWs from deep convection can penetrate well into the thermosphere. We chose a canonical horizontal wind of 20 m s^{-1} in the lower atmosphere in order to impose anisotropy on the GW spectrum. This caused eastward propagating GWs to steepen to higher intrinsic frequencies and larger vertical wavelengths, while westward propagating GWs red-shifted to lower intrinsic frequencies and smaller vertical wavelengths. This resulted in eastward propagating GWs dissipating at higher altitudes than westward propagating GWs. The resulting body forces were found to be $\sim$600 km $\times$ 600 km $\times$ 40–80 km in the x, y, and z directions for the shear used here, and to last for 0.5–1 hours for a single deep plume and for the duration of strong convection for the MCC. Additionally, owing to the shear, the position of maximum forcing is shifted upstream (against the shear) by $\sim$300 km from the source. The body forces achieve maximum amplitudes at $z \simeq 180-200$ km during both extreme solar minimum and active solar conditions. However, the acceleration is $\sim$2 times larger during extreme solar minimum than during active solar conditions. The peak body force altitude resulting from the MCC is lower than that resulting from the single, deep convective plume by $\sim$10–15 km because the GW spectra for the predominantly shallow plumes in the MCC are concentrated at shorter vertical wavelengths, leading to somewhat lower dissipation altitudes. From the location of the thermospheric body forces, we estimate that the contributing GWs likely have intrinsic frequencies close to the buoyancy frequency in the thermosphere, with initial $\lambda_z(z_i) \sim 45-55$ km and $\lambda_x \sim 50-80$ km, and maximum vertical wavelengths (prior to dissipating) of $\lambda_z \sim 75-125$ km during extreme solar minimum. During active solar conditions, we also estimate that the contributing GWs likely have intrinsic frequencies close to the buoyancy frequency in the thermosphere, with initial $\lambda_z(z_i) \sim 25-30$ km and $\lambda_x \sim 60-90$ km, and maximum vertical wavelengths (prior to dissipating) of $\lambda_z \sim 45-55$ km.

[60] During extreme solar minimum, the full width half-max accelerations resulting from a single, deep, convective plume and from the MCC are estimated to be $\simeq$0.15–0.25 m s^{-2} and $\simeq$0.5–0.75 m s^{-2}, respectively, when we take into account the decrease in amplitude by a factor of 2 or 3 if the spectrum had passed through realistic mesospheric and lower thermospheric winds, as discussed below. These accelerations are very large. An acceleration of $\simeq$0.5 m s^{-2} is equivalent to an instantaneous acceleration of 2000 m s^{-1} hr^{-1}. Over the duration of the body

force, the neutrals and ions could be accelerated to very large velocities.

[61] Although the peak altitudes for the body forces were found to be approximately the same during extreme solar minimum and active solar conditions, the altitude profiles were found to differ substantially. During extreme solar minimum, there is insignificant body forcing above $z \sim$ 230 km, whereas during active solar conditions, the body force extends up to $z \sim 360$ km. Thus substantial body forcing and GW presence likely occurs at the highest altitudes during active solar conditions from tropospheric convection.

[62] Although we included a modest lower atmosphere wind in our model, we did not include daily and seasonally varying large mesospheric and lower thermospheric winds. These winds will further filter the GW spectrum before reaching altitudes at which dissipation becomes important. Using typical mesospheric and thermospheric winds, *Hines and Reddy* [1967] estimated that only 30% of the GW energy will reach the ionosphere for GWs having phase speeds of 50 m s^{-1}, while 50–60% of the GW energy will reach the ionosphere for GWs having phase speeds of >100 m s^{-1}. Because the GWs which form the peak of the thermospheric body force in our model during extreme solar minimum and active solar conditions have phase speeds of ~75 and 50 m s^{-1} (VF2004), respectively, we estimated throughout this paper that the strength of the thermospheric body forces would only be 1/2–1/3 of our model values. Because this effect filters GWs with lower phase speeds, the thermospheric body force may instead be located at somewhat higher altitudes where the GWs with somewhat larger phase speeds dissipate. Because the GW spectrum from our convection model is broad, it is likely that differing winds will cause differing portions of a GW spectrum to be most influential in creating a thermospheric body force. Due to the presence in the convective spectrum of GWs having phase speeds in excess of 100 m s^{-1} (VF2004), it is likely that deep convection would always result in GW propagation, dissipating, and momentum flux divergence within the thermosphere.

[63] It is unknown at present what effect these horizontal body forces might have on the thermosphere. However, the effect of localized, intermittent horizontal body forcings when viscous dissipation is unimportant is well known [*Vadas and Fritts*, 2001; *Vadas et al.*, 2003]. In particular, a localized, horizontal wind is generated in the direction of the force with spatial extent of order 1–2 times the full width and of order the full depth of the body force. Additionally, a broad spectrum of secondary GWs which propagate upward and downward with equal amplitudes is excited with spatial and temporal scales characteristic of the body force. For example, if the body force is "fast," the GW spectrum will peak at λ_x, $\lambda_y \sim$ twice the full width, $\lambda_z \sim$ 1–2 times the full depth of the body force. Because the thermospheric horizontal body forces found in this paper have characteristic timescales of $\tau \sim 2\pi L_H/(L_z N) \sim 2$ hours, where L_H and L_z are the horizontal and vertical scales of the horizontal body force, respectively, this force is fast if deep convection lasts for ~2 hours or less. In this case, large-scale secondary GWs might be excited with λ_x, $\lambda_y \sim$ 100–3000 km and $\lambda_z \sim$ 10–400 km with wave periods of 1–6 hours. Those upward propagating secondary GWs with $\lambda_z < 100$ km likely dissipate near the body force, depending on the thermospheric temperature (Vadas, submitted manuscript, 2006). However, those secondary GWs with very large $\lambda_z > 100$ km may propagate to very high altitudes before dissipating, especially during active solar conditions. Downward propagating secondary GWs might be able to propagate reasonably far horizontally before dissipating, although with decreasing wave amplitudes because of density and dissipative effects.

[64] Therefore even though the GWs excited by convection are small-scale and midscale, because wave dispersion broadens the GW spectrum horizontally and temporally, dissipation broadens the spectrum vertically, and the duration of deep convection broadens the spectrum temporally, their dissipation in the thermosphere and accompanying momentum flux divergence results in large-scale, horizontal, thermospheric body forces. These thermospheric body forces may be a new source of midscale and large-scale, long-period, high-altitude, secondary GWs and induced TIDs which would be correlated with lower atmospheric convection (with a time delay of a few hours), and which could occur during magnetically active and quiet times. We also note that any source of lower atmospheric GWs can create momentum flux divergence and body forcing in the thermosphere, provided the intial source contains GWs of sufficient amplitudes and with large enough vertical wavelengths and high enough frequencies to propagate (and dissipate) at high altitudes within the thermosphere. For example, another potential source of GWs which likely dissipates at high altitudes within the thermosphere is secondary GWs created from GW breaking near the mesopause [*Vadas and Fritts*, 2002; *Fritts et al.*, 2002; *Vadas et al.*, 2003].

[65] Indeed, there is some evidence of an unknown source of GWs up to altitudes of $z \sim 200$ km (which are much higher than auroral excitation altitudes) [*Cole and Hickey*, 1981]. Additionally, large perturbations in the atomic oxygen density with large scales of λ_x, $\lambda_y \sim$ 400–4000 km are observed even during low magnetic activity [*Hedin and Mayr*, 1987], and large-scale GWs are observed during quiet geomagnetic conditions [*Mayr et al.*, 1990]. These observations could be explained by these large-scale, secondary GWs, if they are indeed created from thermospheric body forces. It is not presently known what amplitudes these secondary GWs might have. However, when dissipation is unimportant, the secondary wave momentum fluxes vary quadratically with the horizontal body force strength, so larger forcings create much more secondary GWs than smaller forcings [*Vadas et al.*, 2003]. Additionally, very slow forcings, which take much longer than the characteristic timescale to occur, create primarily very long period secondary GWs. In summary, the localized and highly intermittent thermospheric horizontal body forces formed from dissipation of GWs from deep convection are a new, unexplored, and possibly important and intermittent source of neutral horizontal winds and upward and downward propagating secondary GWs in the thermosphere.

[66] **Acknowledgments.** We thank Michael Hickey, Rebecca Bishop, and an anonymous reviewer for helpful comments. This research was supported by the National Aeronautics and Space Administration under contracts NAS5-02036 and NNH04CC67C, the National Science Foundation under grants ATM-0307910 and ATM-0435789, and the Air Force Office of Scientific Research under contract F49620-00-C-0045.

[67] Arthur Richmond thanks Michael Hickey and Frank Djuth for their assistance in evaluating this paper.

References

Banks, P. M., and G. Kockarts (1973), *Aeronomy, Part A*, 430 pp., Elsevier, New York.

Bauer, S. J. (1958), An apparent ionospheric response to the passage of hurricanes, *J. Geophys. Res.*, *63*, 265–269.

Beres, J. H., M. J. Alexander, and J. R. Holton (2002), Effects of tropospheric wind shear on the spectrum of convectively generated gravity waves, *J. Atmos. Sci.*, *59*, 1805–1824.

Cole, K. D., and M. P. Hickey (1981), Energy transfer by gravity wave dissipation, *Adv. Space Res.*, *1*, 65–74.

Cotton, W. R., and R. A. Anthes (1989), *Storm and Cloud Dynamics*, 883 pp., Elsevier, New York.

Crowley, G., T. B. Jones, and J. R. Dudeney (1987), Comparison of short period TID morphologies in Antarctica during geomagnetically quiet and active intervals, *J. Atmos. Terr. Phys.*, *49*, 1155–1162.

Del Genio, A. D., and G. Schubert (1979), Gravity wave propagation in a diffusively separated atmosphere with height-dependent collision frequencies, *J. Geophys. Res.*, *84*, 4371–4378.

Dewan, E. M., R. H. Picard, R. R. O'Neil, H. A. Gardiner, J. Gibson, J. D. Mill, E. Richards, M. Kendra, and W. O. Gallery (1998), MSX satellite observations of thunderstorm-generated gravity waves in mid-wave infrared images of the upper stratosphere, *Geophys. Res. Lett.*, *25*, 939–942.

Djuth, F. T., M. P. Sulzer, J. H. Elder, and V. B. Wickwar (1997), High-resolution studies of atmosphere-ionosphere coupling at Arecibo Observatory, Puerto Rico, *Radio Sci.*, *32*, 2321–2344.

Djuth, F. T., M. P. Sulzer, S. A. Gonzales, J. D. Mathews, J. H. Elder, and R. L. Walterscheid (2004), A continuum of gravity waves in the Arecibo thermosphere?, *Geophys. Res. Lett.*, *31*, L16801, doi:10.1029/2003GL019376.

Einaudi, F., and C. O. Hines (1970), WKB approximation in application to acoustic-gravity waves, *Can. J. Phys.*, *48*, 1458–1471.

Francis, S. H. (1973), Acoustic-gravity modes and large-scale traveling ionospheric disturbances of a realistic dissipative atmosphere, *J. Geophys. Res.*, *78*, 2278–2301.

Fritts, D. C., and M. J. Alexander (2003), Gravity wave dynamics and effects in the middle atmosphere, *Rev. Geophys.*, *41*(1), 1003, doi:10.1029/2001RG000106.

Fritts, D. C., S. L. Vadas, and Y. Yamada (2002), An estimate of strong local body forcing and gravity wave radiation based on OH airglow and meteor radar observations, *Geophys. Res. Lett.*, *29*(10), 1429, doi:10.1029/2001GL013753.

Gossard, E. E., and W. H. Hooke (1975), *Waves in the Atmosphere*, 456 pp., Elsevier, New York.

Hedin, A. E., and H. G. Mayr (1987), Characteristics of wavelike fluctuations in Dynamics Explorer neutral composition data, *J. Geophys. Res.*, *92*, 11,159–11,172.

Hickey, M. P., and K. D. Cole (1987), A quartic dispersion equation for internal gravity waves in the thermosphere, *J. Atmos. Terr. Phys.*, *49*, 889–899.

Hickey, M. P., and K. D. Cole (1988), A numerical model for gravity wave dissipation in the thermosphere, *J. Atmos. Terr. Phys.*, *50*, 689–697.

Hines, C. O. (1960), Internal atmospheric gravity waves at ionospheric heights, *Can. J. Phys.*, *38*, 1441–1481.

Hines, C. O. (1964), Minimum vertical scale sizes in the wind structure above 100 kilometers, *J. Geophys. Res.*, *69*, 2847–2848.

Hines, C. O. (1967), On the nature of travelling ionospheric disturbances launched by low-altitude nuclear explosions, *J. Geophys. Res.*, *72*, 1877–1882.

Hines, C. O. (1968), An effect of molecular dissipation in upper atmospheric gravity waves, *J. Atmos. Terr. Phys.*, *30*, 845–849.

Hines, C. O., and W. H. Hooke (1970), Discussion of ionization effects on the propagation of acoustic-gravity waves in the ionosphere, *J. Geophys. Res.*, *75*, 2563–2568.

Hines, C. O., and C. A. Reddy (1967), On the propagation of atmospheric gravity waves through regions of wind shear, *J. Geophys. Res.*, *72*, 1015–1034.

Hocke, K., and K. Schlegel (1996), A review of atmospheric gravity waves and traveling ionospheric disturbances: 1982–1995, *Ann. Geophys.*, *14*, 917–940.

Hocke, K., and T. Tsuda (2001), Gravity waves and ionospheric irregularities over tropical convection zones observed by GPS/MET radio occultation, *Geophys. Res. Lett.*, *28*, 2815–2818.

Hocke, K., K. Schlegel, and G. Kirchengast (1996), Phases and amplitudes of TIDs in the high-latitude F-region observed by EISCAT, *J. Atmos. Terr. Phys.*, *58*, 245–255.

Horinouchi, T., T. Nakamura, and J. Kosaka (2002), Convectively generated mesoscale gravity waves simulated throughout the middle atmosphere, *Geophys. Res. Lett.*, *29*(21), 2007, doi:10.1029/2002GL016069.

Hung, R. J., and J. P. Kuo (1978), Ionospheric observation of gravity-waves associated with hurricane Eloise, *J. Geophys.*, *45*, 67–80.

Hung, R. J., and R. E. Smith (1978), Ray tracing of gravity waves as a possible warning system for tornadic storms and hurricanes, *J. Appl. Meteorol.*, *17*, 3–11.

Hung, R. J., T. Phan, and R. E. Smith (1978), Observations of gravity waves during the extreme tornado outbreak of 3 April 1974, *J. Atmos. Terr. Phys.*, *40*, 831–843.

Kelley, M. C. (1989), *The Earth's Ionosphere*, 487 pp., Elsevier, New York.

Klostermeyer, J. (1972), Numerical calculation of gravity wave propagation in a realistic thermosphere, *J. Atmos. Terr. Phys.*, *34*, 765–774.

Kundu, P. (1990), *Fluid Dynamics*, 638 pp., Elsevier, New York.

Lane, T. P., and J. C. Knievel (2005), Some effects of model resolution on simulated gravity waves generated by deep, mesoscale convection, *J. Atmos. Sci.*, *62*, 3408–3419.

Lane, T. P., and M. J. Reeder (2001), Modelling the generation of gravity waves by a maritime continent thunderstorm, *Q. J. R. Meteorol. Soc.*, *127*, 2705–2724.

Lane, T. P., M. J. Reeder, and T. L. Clark (2001), Numerical modeling of gravity waves generated by deep tropical convection, *J. Atmos. Sci.*, *58*, 1249–1274.

Larsen, M. F. (2002), Winds and shears in the mesosphere and lower thermosphere: Results from four decades of chemical release wind measurements, *J. Geophys. Res.*, *107*(A8), 1215, doi:10.1029/2001JA000218.

Larsen, M. F., A. Z. Liu, R. L. Bishop, and J. H. Hecht (2003), TOMEX: A comparison of lidar and sounding rocket chemical tracer wind measurements, *Geophys. Res. Lett.*, *30*(7), 1375, doi:10.1029/2002GL015678.

Lighthill, J. (1978), *Waves in Fluids*, Cambridge Univ. Press, New York.

Marks, C. J., and S. D. Eckermann (1995), A three-dimensional nonhydrostatic ray-tracing model for gravity waves: Formulation and preliminary results for the middle atmosphere, *J. Atmos. Sci.*, *52*, 1959–1984.

Mayr, H. G., I. Harris, F. A. Herrero, N. W. Spencer, F. Varosi, and W. D. Pesnell (1990), Thermospheric gravity waves: Observations and interpretation using the transfer function model (TEM), *Space Sci. Rev.*, *54*, 297–375.

Midgley, J. E., and H. B. Liemohn (1966), Gravity waves in a realistic atmosphere, *J. Geophys. Res.*, *71*, 3729–3748.

Ogawa, T., K. Igarashi, K. Aikyo, and H. Maeno (1987), NNSS Satellite observations of medium-scale traveling ionospheric disturbances at southern high-latitudes, *J. Geomagn. Geoelectr.*, *39*, 709–721.

Oliver, W. L., Y. Otsuka, M. Sato, T. Takami, and S. Fukao (1997), A climatology of F region gravity wave propagation over the middle and upper atmosphere radar, *J. Geophys. Res.*, *102*, 14,499–14,512.

Piani, C., D. Durran, M. J. Alexander, and J. R. Holton (2000), A numerical study of three dimensional gravity waves triggered by deep tropical convection, *J. Atmos. Sci.*, *57*, 3689–3702.

Pitteway, M. L. V., and C. O. Hines (1963), The viscous damping of atmospheric gravity waves, *Can. J. Phys.*, *41*, 1935–1948.

Pitteway, M. L. V., and C. O. Hines (1965), The reflection and ducting of atmospheric acoustic-gravity waves, *Can. J. Phys.*, *43*, 2222–2243.

Press, W. H., S. A. Teukolsky, W. T. Vetterling, and B. P. Flannery (1992), *Numerical Recipes in Fortran*, 2nd ed., 963 pp. Cambridge Univ. Press, New York.

Richmond, A. D. (1978), Gravity wave generation, propagation, and dissipation in the thermosphere, *J. Geophys. Res.*, *83*, 4131–4145.

Röttger, J. (1977), Atmospheric gravity waves generated by penetrative cumulus convection in the tropics, paper presented at 11th Technical Conference on Hurricanes and Tropical Meteorology, Am. Meteorol. Soc., Miami Beach, Fla.

Sentman, D. D., E. M. Wescott, R. H. Picard, J. R. Winick, H. C. Stenbaek-Nielsen, E. M. Dewan, D. R. Moudry, F. T. Sao Sabbas, M. J. Heavner, and J. Morrill (2003), Simultaneous observations of mesospheric gravity waves and sprites generated by a midwestern thunderstorm, *J. Atmos. Sol. Terr. Phys.*, *65*, 5.

Song, I.-S., H.-Y. Chun, and P. P. Lane (2003), Generation mechanisms of convectively forced internal gravity waves and their propagation to the stratosphere, *J. Atmos. Sci.*, *60*, 1960–1980.

Taylor, M. J., and M. A. Hapgood (1988), Identification of a thunderstorm as a source of short period gravity waves in the upper atmospheric nightglow emissions, *Planet. Space Sci.*, *36*, 975–985.

Vadas, S. L., and D. C. Fritts (2001), Gravity wave radiation and mean responses to local body forces in the atmosphere, *J. Atmos. Sci.*, *58*, 2249–2279.

Vadas, S. L., and D. C. Fritts (2002), The importance of spatial variability in the generation of secondary gravity waves from local body forces, *Geophys. Res. Lett.*, *29*(20), 1984, doi:10.1029/2002GL015574.

Vadas, S. L., and D. C. Fritts (2004), Thermospheric responses to gravity waves arising from mesoscale convective complexes, *J. Atmos. Sol. Terr. Phys.*, *66*, 781–804.

Vadas, S. L., and D. C. Fritts (2005), Thermospheric responses to gravity waves: Influences of increasing viscosity and thermal diffusivity, *J. Geophys. Res.*, *110*, D15103, doi:10.1029/2004JD005574.

Vadas, S. L., D. C. Fritts, and M. J. Alexander (2003), Mechanism for the generation of secondary waves in wave breaking regions, *J. Atmos. Sci.*, *60*, 194–214.

Volland, H. (1969a), The upper atmosphere as a multiply refractive medium for neutral air motions, *J. Atmos. Terr. Phys.*, *31*, 491–514.

Volland, H. (1969b), Full wave calculations of gravity wave propagation through the thermosphere, *J. Geophys. Res.*, *74*, 1786–1795.

Waldock, J. A., and T. B. Jones (1986), HF doppler observations of medium-scale travelling ionospheric disturbances at mid-latitudes, *J. Atmos. Terr. Phys.*, *48*, 245–260.

Waldock, J. A., and T. B. Jones (1987), Source regions of medium scale travelling ionospheric disturbances observed at mid-latitudes, *J. Atmos. Terr. Phys.*, *49*, 105–114.

Yanowitch, M. (1967), Effect of viscosity on gravity waves and the upper boundary condition, *J. Fluid Mech.*, *29*, 209–231.

Yeh, K. C., C. H. Liu, and M. Y. Youakim (1975), Attenuation of internal gravity waves in model atmospheres, *Ann. Geophys.*, *31*, 321–328.

Zhang, S. D., and F. Yi (2002), A numerical study of propagation characteristics of gravity wave packets propagating in a dissipative atmosphere, *J. Geophys. Res.*, *107*(D14), 4222, doi:10.1029/2001JD000864.

D. C. Fritts and S. L. Vadas, Colorado Research Associates, NorthWest Research Associates, 3380 Mitchell Lane, Boulder, CO 80301, USA. (vasha@cora.nwra.com)